EXPERIMENTAL INVESTIGATION OF BREAKING WAVES ON BEACHES

by

LISA SMITH

THESIS

for the degree of

MASTER OF SCIENCE

(Master i Anvendt matematikk og mekanikk)

Faculty of Mathematics and Natural Sciences
University of Oslo

November 2014

Det matematisk- naturvitenskapelige fakultet
Universitetet i Oslo

Abstract

This master thesis presents an experimental study of plunging breakers on a beach with a slope of 5.1°. The incoming waves are solitary waves with various amplitudes, and the areas investigated are the swash zone and the plunge point. The purpose of this thesis was to answer some of the questions regarding wave breaking. Surface elevation, velocities close to the beach, maximum run-up and surface profiles have been studied.

The experimental investigation revealed that the plunging jet behaved like a stagnation flow at the plunge point. Stretching of the jet was obtained near the boundaries. The motion in the swash zone seemed to be more turbulent as we moved further up the beach. The up-rush motion seemed to be more turbulent than the backwash motion.

Acknowledgements

First I would like to thank my supervisors Professor Atle Jensen, Professor Geir K. Pedersen and pre Dr. Erika Lindstrøm. Their comments and advice has been highly appreciated. Thanks for all the help I received during this thesis. I would especially like to thank Atle, my main supervisor for suggesting this exciting topic. Erika taught me everything about the experimental set-up and motivated me throughout the entire process. While working in the laboratory, I got a lot of help from the laboratory engineer Olav Gundersen. He made the beach in the wave tank and lectured me in the proper ways to turn a screw. I also got help from the former laboratory engineer Svein Vesterby who helped me with the bed shear stress measurements. Thanks to both of you. Terje Kvernes, the local IT support, helped me with small and big computer problems. Thank you. I will also like to thank Dr. Jostein Kolsaas who has answered a large amount of questions regarding experimental set-up and image processing methods. I am especially grateful for all the love and support I received from my family and my boyfriend Sjur during this process.

Contents

Chapter 1

Introduction

1.1 Thesis objectives

Ocean waves that travel towards the shore will steepen, and at some point close to the shore breaking may occur. Wave breaking is an important topic since it can generate enormous loads on vessels and offshore structures, which can result in enormous destruction on the bodies. Breaking waves also have a large impact on sediment transport onshore. The sediment transport can result in erosion on cliffs and deformation of the shoreline. Although breaking waves is a well-known phenomenon from our daily life, many physical aspects regarding wave breaking are still poorly understood. No analytical theory is able to predict the post stages of wave breaking.

The main focus of this thesis is to find out which physical quantities we are able to measure after waves have broken. And since little is known about the physics, a broad approach is needed. The main idea was to investigate physical quantities such as as bed shear stress, fluid velocities, surface profiles of the run-up, and maximum run-up. However only the last three quantities was investigated, due to difficulties regarding the measuring equipment for the bed shear stress.

1.2 Background

Several experimental studies of breaking waves have been performed in the latest years. A brief introduction of some studies is presented in the following.

Jensen et al. (2003) performed an experimental investigation of wave run-up at a steep beach, where Particle Image Velocimetry (PIV) was performed when the wave front was at its steepest. They compared the measurements with a Boussinesq model. The beach slope was 10.54°. They found that the waves with the largest amplitude was close to breaking, since a part of the wave front almost formed a plunging jet.

Petti and Longo (2001) did turbulence experiments of plunging and collapsing breakers. The experiments were carried out in a 48m long and 0.8m wide flume. They used a Laser Doppler Velocimetry (LDV) to measure instantaneous velocities. The velocities were measured 0.5mm above the beach bed. They concluded that turbulent energy is higher during up-rush than backwash.

(Cowen et al., 2003) used PIV with fluorescent particles to investigate the swash zone. The fluorescent particles enabled them to investigate areas where the flow was affected by air bubbles. They generated both spilling and plunging breakers with a period T=2.0s. They found that the up-rush turbulence was dominated by the bore, while the backwash was dominated by wall bounded turbulence. The experiment was conducted in a 32m long and 0.6m wide wave tank, with a beach slope with an inclination of 1:20.

A large and medium scale measurement of bed shear stress in bore driven swash was conducted by Barnes et al. (2009). They used a shear plate, based on a shear cell developed by Grass et al. (1995). The surface of the shear plate was smooth and with dimensions 10cm x 20cm. The medium scale experiment was done in a 20m long and 0.45m wide flume. The slope was 1:10 and two different grades of roughness were employed at the beach. The large scale experiment was done in a 20m long and 0.85m wide flume. Experiments were done with different roughness and the beach had a slope of 1:12. The results revealed that the bed shear stress had its maximum value at the bore arrival and then decreased with time. The backwash maximum was about 2-4 times less than the up-rush maximum, which is in accordance to Cowen et al. (2003).

O'Donoghue et al. (2010) used PIV to investigate velocities in breaking waves at beaches generated by a dam-break. Fifty repetitions were used to estimate an ensemble average. One of the results is that the turbulent kinetic energy seems to be larger for up-rush than back-wash.

Kikkerta et al. (2011) did measurements on a bore driven swash. The experiments were carried out in a 20m long flume with a width of 0.45m. They used PIV to measure velocities and Laser-Induced Fluorescence (LIF) to measure the water depth. The beach slope was 1:10 and the experiments were repeated on beaches with different roughness. This study concludes that the up-rush friction factors are smaller than friction factors for backwash. This contradicts the findings from the work done by Cowen et al. (2003) and Barnes et al. (2009).

Rivillas-Ospina et al. (2012) used Bubble image Velocimetry (BIV) to investigate velocity fields in the swash and surf zone for plunging breakers. A numerical model based on Reynolds Average Navier Stokes (RANS) equation was used to compare the measurements. Rivillas-Ospina et al. (2012) found that the BIV measurements were in agreement with the RANS model.

None of the aforementioned studies have a high resolution near the beach bed or captures velocities in the front of the swash tongue. Measurements where the amplitude of the breaking waves varies have not been conducted. My contribution is an attempt to investigate these unknown fields.

1.3 Content of thesis

This thesis starts with a short introduction of theory regarding solitary and breaking waves in Chapter 2. Definitions and descriptions of the waves will be provided there. Chapter 3 includes a theoretical description of the measuring methods used in this thesis. A short introduction to Particle Image Velocimetry (PIV), Particle Tracking Velocimetry (PTV) and the theory behind the ultrasonic probes will be given. Chapter 4 consists of a practical description of the experiments, information regarding the experimental set-up, as well as information regarding the post processing. A detailed description of the beach and a discussion regarding its properties will be discussed in chapter 4. The results from PIV, PTV, maximum run-up, and surface profiles of the run-up are provided in chapter 5. Also the effect of the joints between the PETG plates will be discussed. A brief summary and discussion is provided in chapter 6. At the end of this chapter suggestion of future work can be found.

The appendices are divided into two parts. The first part is a report on a bed shear stress measuring device. The idea was to validate the

device in a known environment, pipe flow. However the outcome was not as expected. The report is given in appendix A. The second part of the appendices is results from some post processing of external data. A comparison of MatPIV and DigiFlows PIV code performed on linear waves is given. Velocities and acceleration in plunging breakers in the surf zone is elaborated in this part.

Chapter 2

Theory

Motion of a Newtonian fluid is described by Navier Stokes equation:

$$\frac{\partial \mathbf{v}}{\partial t} + (\mathbf{v} \cdot \nabla)\mathbf{v} = \frac{1}{\rho}\nabla p + \nu \nabla^2 \mathbf{v} + \mathbf{f} \tag{2.1}$$

, where $\mathbf{v}$ is the velocity vector, ρ is the fluid density and $\mathbf{f}$ is a volume force. The equation is derived from conservation of momentum. If the fluid is incompressible, the continuity equation can be derived from conservation of mass.

$$\nabla \cdot \mathbf{v} = 0 \tag{2.2}$$

The boundary conditions at the surface for gravity waves are given in 2.3. Surface tension is neglected and the fluid is assumed to be inviscid.

$$\begin{aligned} p &= p_{atm} \quad at \quad z = \eta \\ \frac{D\eta}{Dt} &= w \quad at \quad z = \eta \end{aligned} \tag{2.3}$$

The boundary condition for gravity waves at the bottom is given by.

$$\mathbf{v} \cdot \mathbf{n}_b = 0 \quad at \quad z = H(x, y) \tag{2.4}$$

, where the normal vector to the bottom is $\mathbf{n}_b = \nabla(z - H(x, y))$.

2.1 Solitary waves

Solitary waves were first observed by John Scott Russell in 1834. The waves consisted of one single crest and travelled with constant speed without changing shape (Figure 2.1). They are nonlinear and dispersive.

A solution for the surface elevation η of solitary waves can be derived from the Korteweg-de Vries (KDV) equation, which can be derived from Navier Stokes equation 2.1. Assume the relative amplitude α to be small, and the depth H to be much smaller than the characteristic wavelength l. If the fluid is inviscid and incompressible, the Boussinesq equation can be derived from Navier Stokes equation. If the waves are propagating in one direction at a constant depth, the Boussinesq equation can be simplified to the KDV equation given by:

$$\eta_t + c_0(1 + \frac{3}{2}\frac{\eta}{H})\eta_x + \frac{c_0 H^2}{6}\eta_{xxx} = 0 \tag{2.5}$$

, where $c_0 = \sqrt{gH}$. The derivation can be found in Gjevik et al. (2010). One solution to the KDV equation is $\eta = H\zeta(\psi)$ where ζ is given in equation 2.6.

$$\zeta = \alpha sech^2\big((\frac{3\alpha}{4})^{\frac{1}{2}}\psi)\big) \quad where \quad \psi \ = \big(x - c_0(1 + \frac{\alpha}{2})t\big)/H \tag{2.6}$$

It is clear from equation 2.6 that the surface elevation is only dependent on the amplitude. So solitary waves can easily be classified, and are therefore preferable to work with experimentally. A full potential solution for solitary waves was found by Tanaka (1986), while Fenton (1972) found a ninth order approximative solution for solitary waves. In this thesis a fourth order approximation by Fenton, and the Tanakas full potential solution will be used.

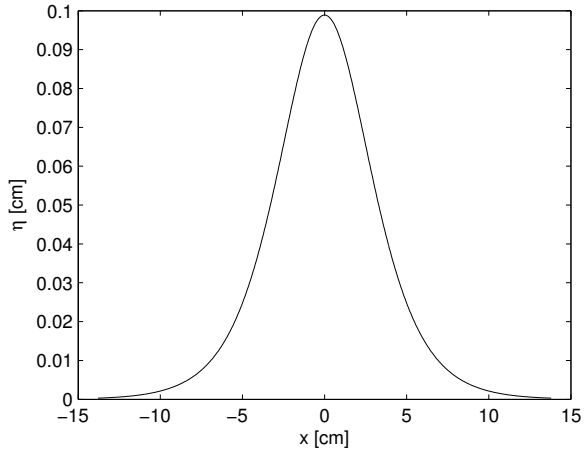

Figure 2.1: *Solitary wave with amplitude 0.1cm. The solution is calculated from Fenton's fourth order approximation.*

2.2 Breaking waves

On constant depth, the nonlinear effect and dispersion will be balanced for solitary waves (Peregrine, 1983). If the depth decreases as the wave travels towards the shoreline, shallow water steepening will occur. The front of the wave will steepen, which could result in wave breaking. Grilli et al. (1997) has analysed breaking criterion for solitary waves on slopes. They found that no solitary wave would break if the beach slope is higher than 12°. However, if the beach slope is 1:10 (5.1°), the waves will break if $\frac{A}{H} > 0.15$, where A is the solitary wave amplitude when the wave travels on a uniform depth, and H is the water depth.

There are four main types of breaking waves described by Peregrine (1983): *spilling*, *plunging*, *collapsing* and *surging* breakers (Figure 2.2). The breaker type depends on the initial energy of the wave, and the characteristics of the beach slope. A *spilling breaker* can be characterized by white water tumbling down from the wave crest to the front face of the wave. The breaking can occur for a long time. The beach slope is gentle and the waves are steep. *Plunging breakers* are breakers where the wave crest is deformed to an overturning jet. This breaker type is common on beaches with steep slopes. *Collapsing breakers* are breakers where the lower part of the wave crest overturn, and is an intermediate case between *spilling* and *plunging breakers*. *Surging* are breakers where the surface remains smooth during breaking. They appear when the waves have a very gentle slope.

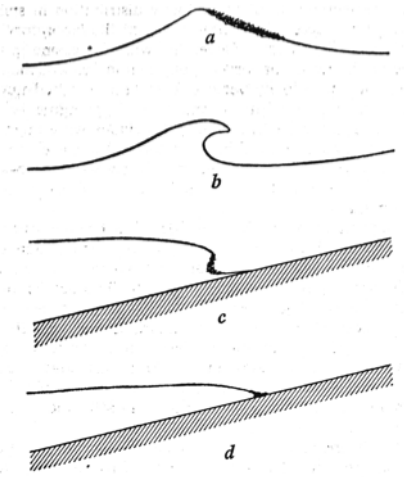

Figure 2.2: *Figure of different breaker types. a) Spilling b) Plunging c) Collapsing and d) Surging breakers (Cokelet, 1977)*

2.2.1 Plunging breakers

In this thesis only plunging breakers will be generated. The surf zone is defined as "The area offshore where waves break, between the outermost breaker and the limit of wave uprush" (*Dictionary.com Unabridged*, 2014). For plunging breakers this will correspond to the area where the wave develops a plunge, to the point where the run-up on the beach starts. The point where the plunger hits the calm water is called the plunge point (Peregrine, 1983). However, in this thesis the plunging breakers hit the beach above still water level. Hereafter the point where the plunger hits the beach is referred to as the plunge point.

After reaching the plunge point, the plunge will be deformed into a swash tongue. Swash is defined as "a forward pulse of water released by a breaking wave after it has broken, capable of moving sand up the beach" (Smithson et al., 2002). So for plunging breakers, the swash zone is the area located between the plunge point and maximum run-up.

Chapter 3

Measurement techniques

In this thesis the surface elevation of breaking waves was measured with ultra-sonic acoustic probes. Velocity fields were investigated by Particle Image Velocimetry (PIV) and Particle traking Velocimetry (PTV). A brief introduction to the measuring techniques will be given in the following.

3.1 Quantitative imaging techniques

Quantitative imaging techniques are often used to investigate fluid dynamics (Sveen and Cowen, 2004). These techniques can characterize fluid motion close to boundaries and free surfaces. They are optical measurement techniques, and can be divided into two main groups. The first group consists of techniques where the flow is seeded with a continuous dye, whereas the second group consists of techniques where the flow is seeded with passive particles. PIV and PTV belongs to the latter group.

There are two main descriptions of fluid motion, Eulerian and Lagrangian representations. The Eulerian representation describes flow properties of a fluid at fixed spatial positions. The Lagranginan is an expansion of single particle kinematic, where the trajectories of single particles are followed (Kundu et al., 2012).

3.1.1 Particle Image Velocimetry

This introduction to PIV is based on a summary article written by Sveen and Cowen (2004). PIV is a pattern matching technique that calculates velocity fields in fluids, based on an Eulerian representation of fluid motion. The fluid is seeded with particles, which are passive

with respect to the fluid. The particles are illuminated by a light source. The light is sent through a slit, such that a 2D light sheet is shown in the field of interest. A digital camera captures images of the *field of view* (FOV), with a Δt time difference between the images. Once a particle has moved a displacement $\Delta \mathbf{x}$, from one image to another, the velocity can be calculated $\mathbf{u} = \frac{\Delta \mathbf{x}}{\Delta t}$.

Two images are dived into subwindows of size MxN pixels. The size of the subwindows must be large enough, so at least 4 to 5 particles are contained in each subwindow. The subwindows must also cover the largest particle displacement.

There are two methods used to find the displacement of a particle in the FOV. The most common is single-exposure multiple images, which uses cross-correlation analysis to find the displacement. The cross correlation function of two corresponding square subwindows F'_{IJ} andF''_{IJ} is given by:

$$R(s,t) = \frac{1}{N^2} \sum_{i=0}^{N-1} \sum_{j=0}^{N-1} \{F'_{I,J}(i,j)\}\{F''_{I,J}(i+s, j+t)\} \qquad (3.1)$$

where F'_{IJ} is the the I,J subwindow of the first image, and F''_{IJ} is the corresponding subwindow from the second image. The indices (i, j) correspond to a pixel location, (r, s) correspond to a sought displacement, and $R(s, t)$ is the cross correlation plane. The location difference between the center of the correlation plane and the highest correlation peak is the most obtained displacement.

If the actually displacement x is larger than N/2 pixels, the correlation peak will alias to the location $-(N - x)$. If the displacement is bigger than N pixels, no particles from the first subwindow can be detected in the second subwindow, and the correlation peak in the correlation plane will represent a random correlation of two uncorrelated subwindows. The correlation plane can be separated into three layers. The correlation of the mean background intensities $R_b(s, t)$, the correlation between mean and fluctuating intensities $R_f(s, t)$, and the correlation between the fluctuating intensities $R_d(s, t)$. The last one contains the actual displacement peak, and can be found by calculating a normal-

ized correlation given by:

$$\hat{R}(s,t) = \frac{1}{N^2} \frac{\sum_i \sum_j \left[F'(i,j) - \overline{F'}\right] \left[F''(i+s,j+t) - \overline{F''}\right]}{\sum_i \sum_j \left(\left[F'(i,j) - \overline{F'}\right]^2 \left[F''(i+s,j+t) - \overline{F''}\right]^2 \right)^{1/2}} \tag{3.2}$$

where $\overline{F'}$ and $\overline{F''}$ is the mean of $F'(i,j)$ and $F''(i+s,j+t)$. The range of $\hat{R}(s,t)$ is 0 to 1, where 1 indicates strong correlation between subwindow F' and F''.

To be able to find the exact location of the center of a particle, we need the particle to cover at least 2-4 pixels. The exposure time of the camera must also be set, such that the particle center can be determined by looking at the intensity of each pixel the particle covers. We want the center pixels to have higher intensity than pixels on the boundaries of particles.

One problem with this method is peak-locking, where the displacement of a particle always is locked to whole pixels. If the actual displacement is 3.4 pixels, the displacement will be locked to 3 pixels, which gives an error of 11%. Peak-locking can be solved by using curve fitting on the displacement peak and the neighbouring peaks, to estimate an exact displacement. Gaussian peak fit is often used and is a good approximation for spherical particles. Another way to solve peak-locking is to dynamically shift the subwindows so the sub-pixel displacement converges to zero.

Each subwindow pair generates one velocity vector. To validate the vectors, two criteria must be fulfilled. Good signal quality and smoothness in both time and space. Vectors can be filtered by setting threshold on the signal to noise ratio (SNR). This is the ratio between the highest correlation peak to the second highest peak in the correlation plane, where the threshold is often set in the range of 1.2-1.5. Local and global filters are often applied. Global mean filters compare a vector to the mean of all the vectors collected in an image pair. Local filters compare a vector to its surrounding vectors. The median is often used, as outliers affect the mean dramatically.

3.1.2 Particle Tracking Velocimetry

The information served in this section is based on Dalziel (2006). PTV tracks individual particles instead of particle pattern as in PIV, and

the technique is based on a Lagrangian representation of fluid motion. The set-up is the same as for PIV, but the seeding density can be less than for PIV.

The main challenge with PTV is to locate the same particle in two images without interference from other particles. The mean distance between particles must therefore be larger than the maximum expected displacement. First, particles need to be located in the two images. This can be done by scanning the images and setting a threshold on light intensity, size, and shape to decide whether a blob is a particle or not. When all particles are found in the first image F' and in the second image F'', an algorithm is needed to pair the particles.

Dalziel (1992) found a good approach using a *transportation algorithm* to pair the particles. If properties of the particles in image F' is stored into p_i, and properties of the particles in image F'' are stored into q_j, then an association variable a_{ij} can be defined. If particle p_i corresponds to the particle q_j, the association variable is equal to one, otherwise it is set to zero. One particle in the first image can only correspond to one particle in the next image. This constraint must be applied to the association variable a_{ij}. A cost c_{ij} is also defined, where particle pair properties like differences in light intensity, shape, and distance are compared. The degree of match between particle p_i and q_j is stored as a number in c_{ij}, where c_{ij} equal to zero corresponds to coinciding particles. An objective function Z is defined in equation 3.3.

$$Z = \sum_i \sum_j a_{ij} c_{ij} \tag{3.3}$$

Equation 3.3 must be solved for the association variable a_{ij} as Z get minimized. A small Z will correspond to an overall good matching of all the particles in the images. The association variable will then give the best matching of particles. The seeding density can be increased if more particle properties are taken into account in the cost c_{ij}. An example of a cost where the particle history is stored is given by:

$$c_{ij} = \Phi(p_i) + \sum_f max\Big(0, \omega_f(p_i)\zeta_f(p_i, q_j) - \tau_f\Big) \tag{3.4}$$

,where $\Phi(p_i)$ is zero if information is available from earlier images, and larger than zero otherwise. All the particle characteristics f should be summarized. $\omega_f(p_i)$ represents the cost unit, τ_f is the threshold level for each particle characteristics, and $\zeta_f(p_i, q_j)$ represents the cost

function. The basic cost function, based on distances between particles is:

$$\zeta_x(p_i, q_j) = |\mathbf{x}_i + \mathbf{u}\Delta t - \mathbf{x}_j|^2 \tag{3.5}$$

The velocity $\mathbf{u}$ is a prediction based on history from the particle p_i. If no history is available an initial guess is set. When the correct particles are paired, the velocity of the particles can be calculated by, $\mathbf{u}(x, y, t) = \frac{\Delta \mathbf{x}(x,y,t)}{\Delta t}$. This method is more efficient than PIV, but velocity vectors are random spatial distributed. One particle gives one velocity vector. To get the same spatial resolution as achieved with PIV, the vectors must be interpolated on to a grid. This is the main criticism of PTV (Sveen and Cowen, 2004). If the subwindow size in PIV decreases to contain only one particle, PIV will converge to PTV.

3.2 Surface elevation and still water level measurements

The surface elevation and the still water level are measured with ultra sonic gauges. The gauges send an ultra sonic signal towards a surface. The signal is then reflected at the surface, and a sensor picks up the reflected signal. The signal travels through air with the speed of sound. Therefore the distance from the sensor to the surface can be calculated from:

$$D = \frac{c \cdot t}{2}. \tag{3.6}$$

, where c is the speed of sound and t is the time between departure and arrival of the signal. A more detailed description can be found in Banner (2010).

Chapter 4

Practicalities

In this chapter the practical details regarding the experiments will be given. The experiments are divided into a main experiment and two smaller experiments. The main experiment was conducted to find the velocities within the fluid. The other two experiments were performed to find maximum run-up and large scale surface profiles of the run-up. A detailed description of the beach will also be given. Finally the fluid's properties will be discussed.

4.1 Experimental overview

All experiments were conducted in the hydrodynamic lab at UiO. Solitary waves were generated in a 25m long and 0.51m wide wave tank with a piston type wave paddle as described in Jensen et al. (2003). A beach was mounted into the tank with an inclination of 5.1°. The water depth was kept constant at 0.205m.

An acoustic wave gauge (ultra Banner U-Gage S18U) kept track of the water level, while another gauge measured the incoming waves. The sample frequency was 200Hz, and the incoming waves were measured for all cases. Origo was defined as the point where the still water level and the beach intersected. Two coordinate systems were introduced, one parallel to the still water level (x', z'), and one parallel to the beach (x, z) (Figure 4.1). Distances regarding the the set-up are given in Table 4.1.

The waves were classified by their relative amplitude. The wave paddle generated waves with relative amplitude $\frac{A}{H} \approx 0.10, 0.12, 0.20, 0.30, 0.40$ and 0.50. From now on these waves will be referred to as case 10, 12, 20, 30, 40 and 50. Three repetitions were done in all the experiments

The start of the beach	529.81 cm
Water level probe	506.45 cm
Wave probe	486.11 cm
Origo	754.20 cm

Table 4.1: *Distance from the wave paddle to:*

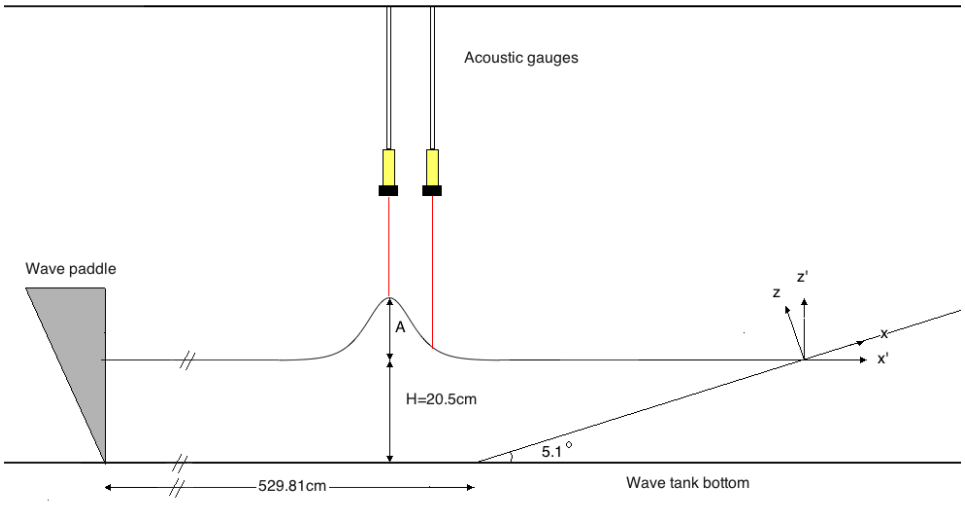

Figure 4.1: *Experimental set-up.*

for all cases.

4.2 The Beach

The beach was made by Olav Gundersen (Lab engineer at the hydrodynamic lab) with help from me. The beach consisted of four pieces of PETG (Polyethylene Terephthalate Glycol-modified) plates with a thickness of 8mm and a width of 50.5cm. The overall length was 7m. The effect of the roughness of PETG plates is documented in Pedersen et al. (2013). The beach was supported by two steel beams, which were mounted in the wave tank. At the start of the beach, the plates were supported by plastic beams. The plastic beams were cut such that the tip of the beach had an inclination of 5.1°. The PETG plate closest to the tank bottom was milled at the start, such that the plate tip corresponded to an inclination of 5.1°. The tip of the milled plate should ideally be infinitely thin, but the tip was 1.5mm thick. Silicone was applied at the tip to avoid a sharp edge between the bottom of the

tank and the beach. The four PETG plates were attached to the steel and plastic beams with silicone. Neoprene sealing strips were applied between the glass walls in the tank and the PETG plates. The strips were 0.3mm and 0.6mm thick.

There were some problems with the joints between the PETG plates. The joints were located at -203,7cm, -9.8cm and 195.5cm shoreward from origo. On the joint at -9.8cm there was a height difference between the two plates. This created a step down from the first plate to the second plate. Silicone was applied to smooth out the sharp edge. Measurements showing this effect were conducted.

PETG is a bendable material. The beach deflected due to its own weight and due to the weight of the overlying water. The maximum deflection of the beach was measured for different values of x. The measurements were performed using a straightedge and feeling gauge. The results are given in Table 4.2.

Distance from origo, x	**Bending of the beach**
0.0 m	2.5 mm
0.5 m	2.7 mm
1.0 m	3.2 mm
1.5 m	3.2 mm
2.0 m	3.4 mm
2.5 m	2.6 mm
3.0 m	2.8 mm

Table 4.2: *Maximum bending of the beach.*

The beach had its highest points close to the side walls in the tank. The lowest point was located in the middle of the beach, and corresponded to maximum bending.

4.3 Experimental set-up for the main experiment

First, the water in the tank was seeded with 50μm polymid particles. The particles were illuminated in a light sheet by a Quantronix Darwin Duo pulsed laser. A Photron SA5 high speed camera synchronized with the laser, captured images of the illuminated particles. The images were captured with a pixel resolution of 1024 x 1024. Images were collected at 3000 frames per seconds (fps) for all cases. Six different field of views

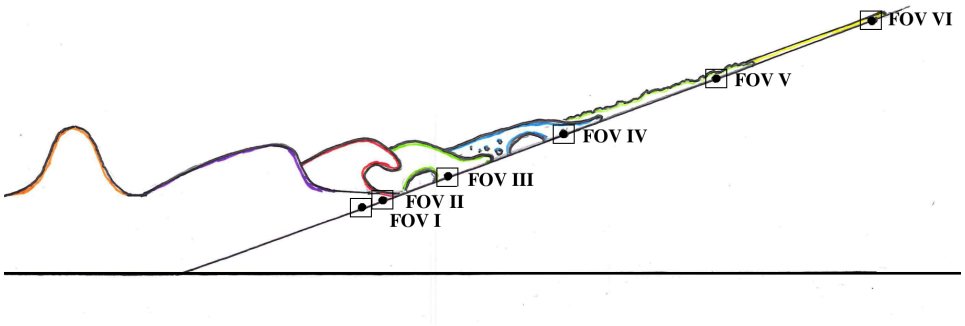

Figure 4.2: *Sketch of the experiment. An example of how plunging breakers evolve with time. The position of the FOVs are properly scaled with respect to the still water level*

(FOV) were located along the beach(Figure 4.2). The exact location for each FOV is given in Table 4.3.

FOV:	I	II	III	IV	V	IV
Location, x:	[-14.08 - -9.82]	[-7.87 - -3.55]	[8.49 - 13.04]	[36.35 - 40.26]	[77.55 - 81.53]	[117.76 - 121.80]
Location, z:	[-2.27 - -1.95]	[-1.81 - 2.52]	[-0.05 - 3.78]	[-0.16 - 3.54]	[-0.04 - 3.79]	[-0.85 - 3.09]

Table 4.3: *Location of the different FOVs in cm. The dimensions of the FOVs are approximately 4cm x 4cm.*

4.3.1 Image processing

The image processing was executed in DigiFlow developed by Dalziel Research Partners. Both PIV and PTV were performed on images captured in the main experiment. The post processing was performed in MATLAB developed by MathWorks.

PTV was performed with *default* setting in DigiFlow. This provided 3087 velocity vectors per frame for case 10, run 1 at FOV3. The number of particles detected by PTV seems to be in agreement with visual inspection. A second order Savitzky-Golay smoothing filter was applied with differential filter size 5.

PIV was performed with various filters applied, including a global, a local and a noise filter. Invalid vectors were interpolated spatially. PIV was performed using interrogation windows of 32 x 8 pixels with a 50% overlap. This subwindow size was chosen to achieve a high resolution in

the z-direction. This was desirable since the boundary layer occurs in a small region near the beach. The rectangular interrogation windows also improve these types of measurements in areas with high velocity gradients. The size of the subwindow is further discussed in Pedersen et al. (2013). An averaging in time was applied where 10 images was used, corresponding to 1/300s.

4.4 Experimental set-up for measuring maximum run-up and surface profiles

First, the experimental set-up regarding maximum run-up will be given. A high speed Photron APX camera was mounted on rails above the beach in the wave tank. A dedolight 400D was used as illumination. The camera was mounted with the same inclination as the beach. First an estimate of maximum run-up was found for all cases. Then the field of views were then chosen, based on these estimates. Every case got its own FOV, and three repetitions were performed for each case. 125 frames per second were used to capture the maximum run-up.

The experimental set-up for measuring the surface profiles was almost the same as in the main experiment. One difference between the set-ups was that the camera stood further away from the wave tank for this experiment, resulting in much larger FOVs. The FOVs from this experiment will be referred to as FOV A and FOV B. They are located at $x = [0 - 60]$cm and $x = [60 - 110]$cm. Another difference from the main experiment was the capturing time. Only 500 fps were used in this experiment, and a weaker continuous dedolight 400D was used as illumination instead of the laser. A white background sheet was attached to the wave tank and the water was dyed dark blue to increase the contrast in the images.

4.5 Experimental difficulties

The main difficulty I would like to point out, is the difficulty regarding an even particle distribution in the fluid. Especially in the front of the wave. The particles seem to slowly sink towards the tank bottom. I had to shovel and stir up particles in between each run. This made the fluid disturbed. The fluid had to calm down before a new run could be conducted. It was hard to balance the time in between the runs, such that the water was calm but had evenly distributed particles. For all runs, extra particles were seeded in the water closest to origo.

Additionally, some issues occurred when focusing the camera. Since most of the FOVs were located above still water level, it was hard to focus the camera in water. The wave paddle ran on maximum effect as often as possible to provide waves with 2cm run-up thickness at FOV VI. The periods with 2cm run-up thickness did not last for long, making the focusing of the camera difficult.

Small parts of silicone loosened from the beach and floated around in the water. They can easily be detected by the camera, but much harder to discover by eye. It was particularly difficult to remove all the siliconee from the water. A specialized tool was made to remove the extra silicone, consisting of a fine gridded fabric tightly applied to a steel frame. This made it much easier.

It should be mentioned that the mean temperature was about $26°C$ during all the experiments. This made the air extremely humid and I assume that this was not the best working condition.

4.6 Viscosity, density and surface tension

At some point during the experiments, I wondered if my experiments could be improved by changing the water in the wave tank. I was afraid the properties of the water had changed, and that air bubbles maintained in fluid for a longer period than for fresh tap water. To investigate the differences between fresh tap water and water from the wave tank, a marble was first dropped into a cylinder filled with tap water, and then into a cylinder filled with water from the tank. The temperature was 26.4°C for the tap water and 26.5°C for the water from the tank. A ruler was attached to the side of the cylinder and a high speed camera captured images of the marble as it moved through the fluids (Figure 4.3). The marble's vertical velocity was calculated, and three repetitions were done. The results are show in Table 4.4.

	Tank water	Tap water
run 1	57.69	59.19
run 2	60.47	60.23
run 3	60.76	60.47

Table 4.4: *Vertical velocities for three repetitions [cm/s]*

The marble seems to achieve the same velocities for fresh tap water and

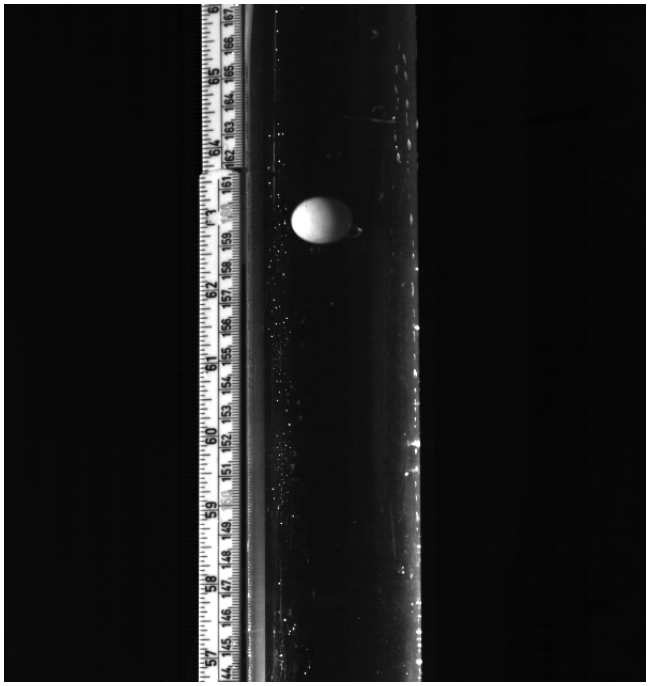

Figure 4.3: *Marble in cylinder filled with water from the tank.*

tank water. This implies that the fluids has about the same viscosity and density. Surface tension has a large impact on the air bubbles, since they can easily be deformed and compressed. The surface tension has not been measured, but a water sample from the experiments has been preserved, in case further investigation is needed.

Chapter 5

Results

In this chapter, results from different aspects of wave breaking will be given. The main focus is kinematics in the swash zone, where velocities in the wave front are emphasized. The plunge point, maximum run-up and surface profiles of the run-up will also be given. The times in this section are denoted with the field of view, t^{FOV}.

5.1 Surface elevation of the incoming waves

The measured dimensionless amplitude of the incoming waves are shown in Table 5.1.

Case:	10	12	20	30	40	50
$\frac{A}{h}$	0.0989	0.1191	0.1981	0.2958	0.3939	0.4874

Table 5.1: *Measured amplitude*

The surface elevation measurements are shown in Figure 5.1. Cubic interpolation is used to filter noise, and linear interpolation is used to filter drop outs. The theoretical solitary surface elevation is provided by Fenton's fourth order approximation for case 10. Tanaka's full potential solution is used for the other cases.

The surface elevation measurements are in agreement with theory, except at the tail of the solitary waves. This can be due to reflection of the waves on the beach. The waves have already been reflected before the tail has arrived at the measuring point, resulting in too high surface elevation at the tail. A boundary integral model will be able to calculate this reflection. This has been done in Lindstrøm (2011), where the tail of the solitary waves are unequal to the front of the waves. Overall, the incoming waves are repeatable and coincide with theory.

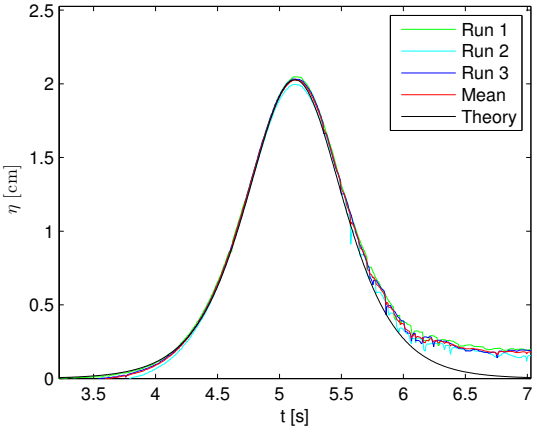

(a) *Case 10*

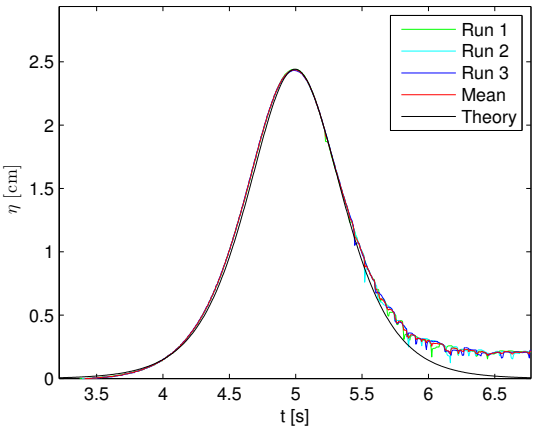

(b) *Case 12*

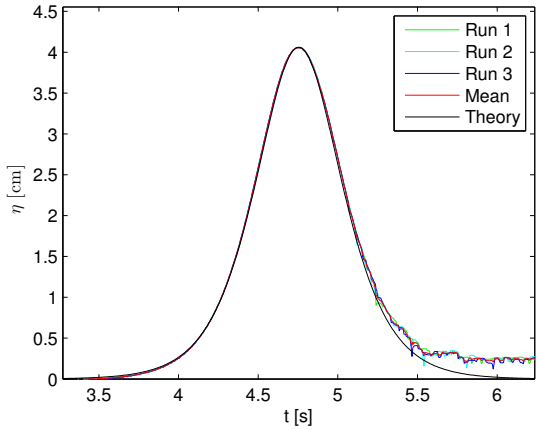

(c) *Case 20*

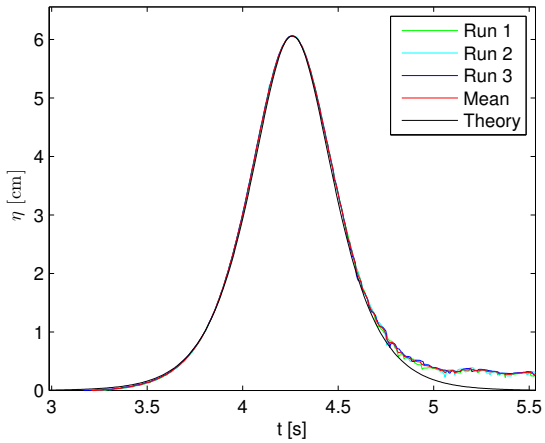

(d) *Case 30*

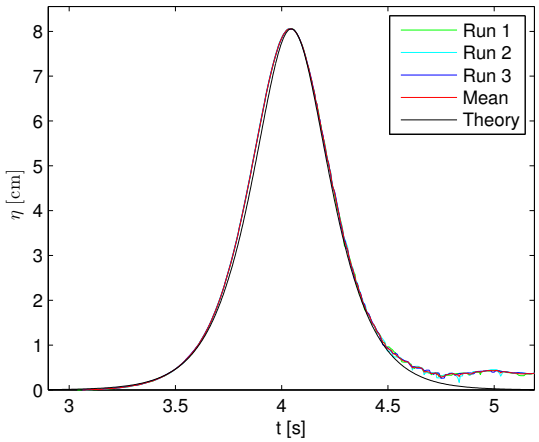

(e) *Case 40*

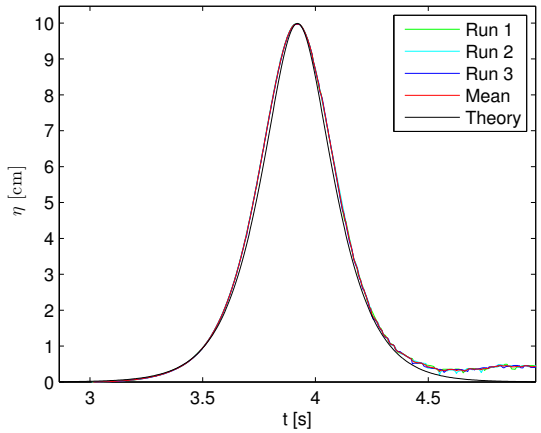

(f) *Case 50*

Figure 5.1: *Surface elevation of incoming waves*

5.2 Effects of the joint between the PETG plates

To investigate effects of the joints on the beach, measurements from FOV I and FOV II will be presented. The beach is made of four PETG plates. This gives us three joints at different locations on the beach. The joint closest to the still water level is located at a critical position ($x = -9.8$)cm. To investigate the influence of this joint, images were captured at locations before (FOV I) and after the joint (FOV II). At some point during the investigation at FOV II, silicone between the PETG plates loosened. Long threads of silicone entered FOV II, creating irregular motion in the boundary layer. The excess silicone was removed and new measurements were performed. All of the three cases are shown in Figure 5.2. PIV was performed on the images as described in Chapter 4.

The outer velocities seem to be unaffected by the joint for all plots in Figure 5.2. If the flow is unaffected by the joint, the upper, middle and bottom velocity profiles should be similar in shape. However, the middle figures are clearly different from the upper and the bottom figures, in the boundary layer. The boundary layer is not as smooth and repeatable for the middle figures, compared to the lower and upper figures in 5.2. The repeatability and smoothness in the boundary layer seems to be improved by removing silicone from the joint. It should be noted that only the velocity profiles from four different times are given, and we can only assume that the flow is not affected by the joint in between these times. Only case 10 and 50 are shown in Figure 5.2. A visual inspection of movies of the other cases supports that this trend is applicable for cases 12 - 40 as well.

(a) *Case 10* (b) *Case 50*

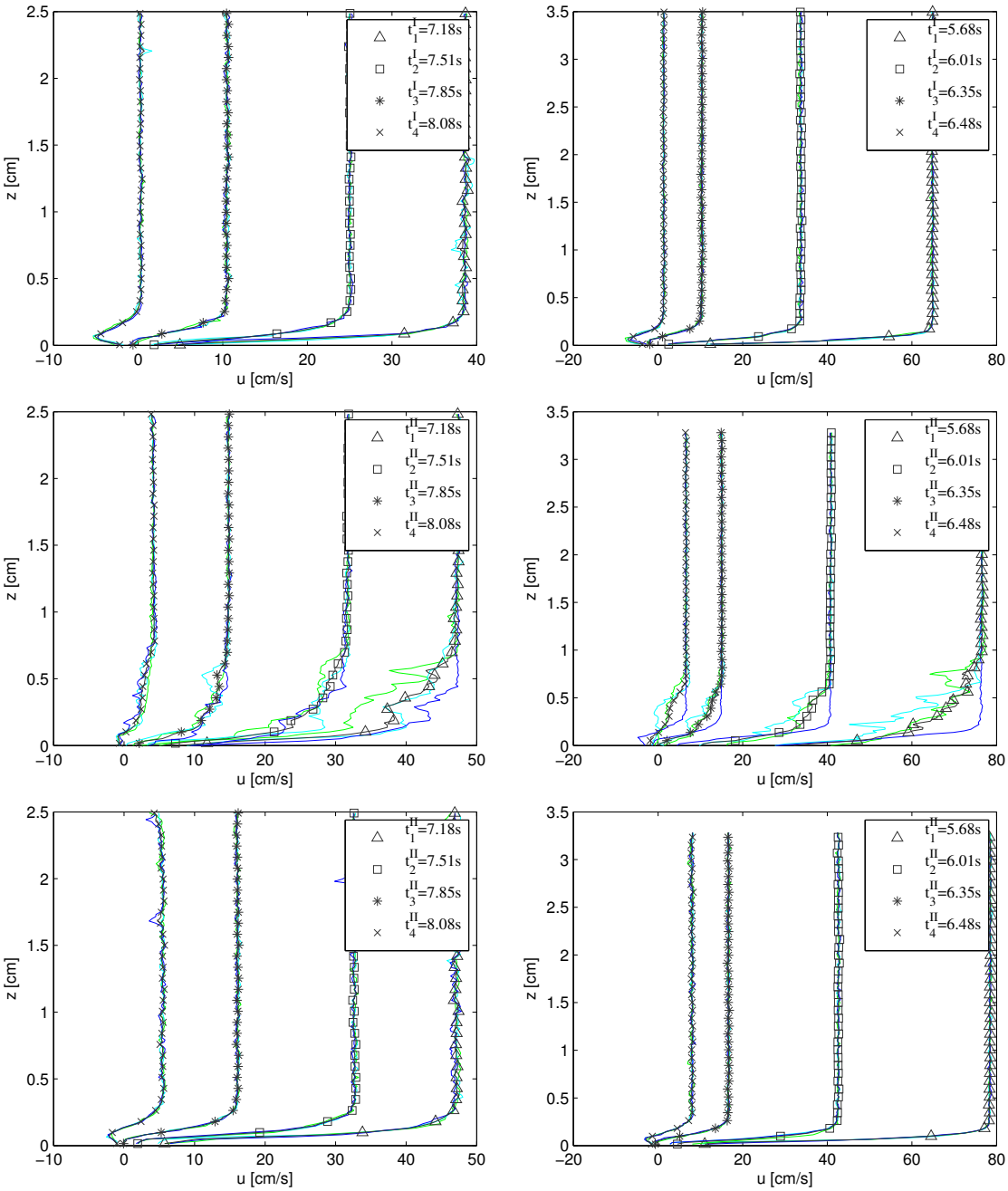

Figure 5.2: *Horizontal velocity profiles.*
Different colors correspond to different runs.
Top: FOV I, velocities before the joint $x_I = -11.00cm$,
Middle: FOV II, velocities before silicone was removed $x_{II} = -5.70cm$
Bottom: FOV II, velocities after silicone was removed $x_{II} = -5.70cm$.

5.3 Velocities close to the plunge point.

In this section experiments from FOV III will be shown. PTV is performed on images captured near the plunge point. The velocities shown in this section correspond to velocities from the first particles obtained in this FOV (Table 5.2).

A MATLAB script was made to estimate when the plunging jet enters the FOV t_p^{III}. The code compares image intensities with intensities from an initial image. When the plunge arrives at the FOV, the intensity difference will start to increase. Figure 5.3 shows how the intensity differences increase for three different runs. A threshold is set to estimate the plunge arrival for the different runs. In this case, the threshold is set to 70, resulting in image number 365, 367 and 354 corresponding to plunge arrival for the different runs. This seems in accordance with visual inspection of the images. Error and results can be found in Table 5.2. The error is small for all the cases, which implies that the breaking event was repeatable in time.

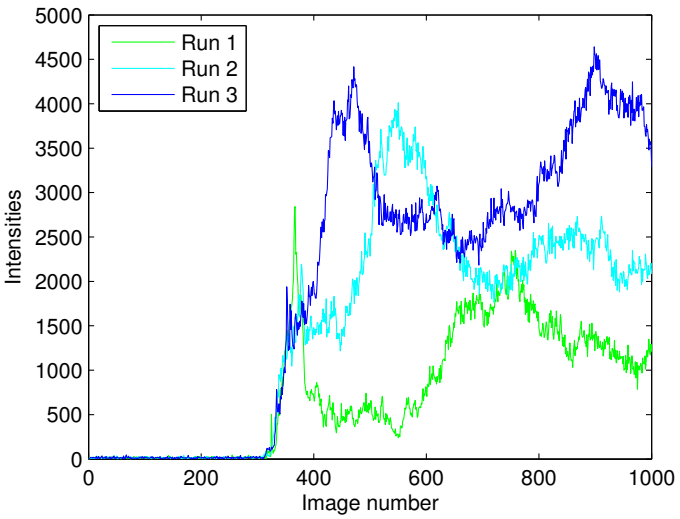

Figure 5.3: *Intesity differences for case 40.*

To investigate kinematics at the plunge point, particle velocities within a strip parallel to the x-axis are plotted in Figures 5.4 to 5.6. The chosen strip corresponds to a region where the outer flow is constant with respect to z.

Figure 5.4 and 5.5 show that the horizontal velocity is linearly dependent of x for cases 10 - 20. The horizontal velocity gradient seems to

increase for increasing wave amplitude. However, the times are different for different cases, and comparison of cases should be performed with caution. Every fourth velocity vector is plotted in the velocity fields in Figures 5.4 to 5.6. Cases 30, 40 and 50 are not linearly dependent of x. Especially the vertical velocity where a minimum can be obtained. The horizontal and the vertical velocities describe stagnation flow with an additional horizontal uniform flow for cases 30, 40 and 50. This means that the plunge itself has a velocity U, and that close to the air bubble, particles have a negative horizontal velocity relative to the plunge. This results in changes in the plunge shape. The plunge stretches in both positive and negative x-direction near the boundary. Overall, the figures show that averaging over x should be performed with caution and that the velocities seem to be repeatable for all cases.

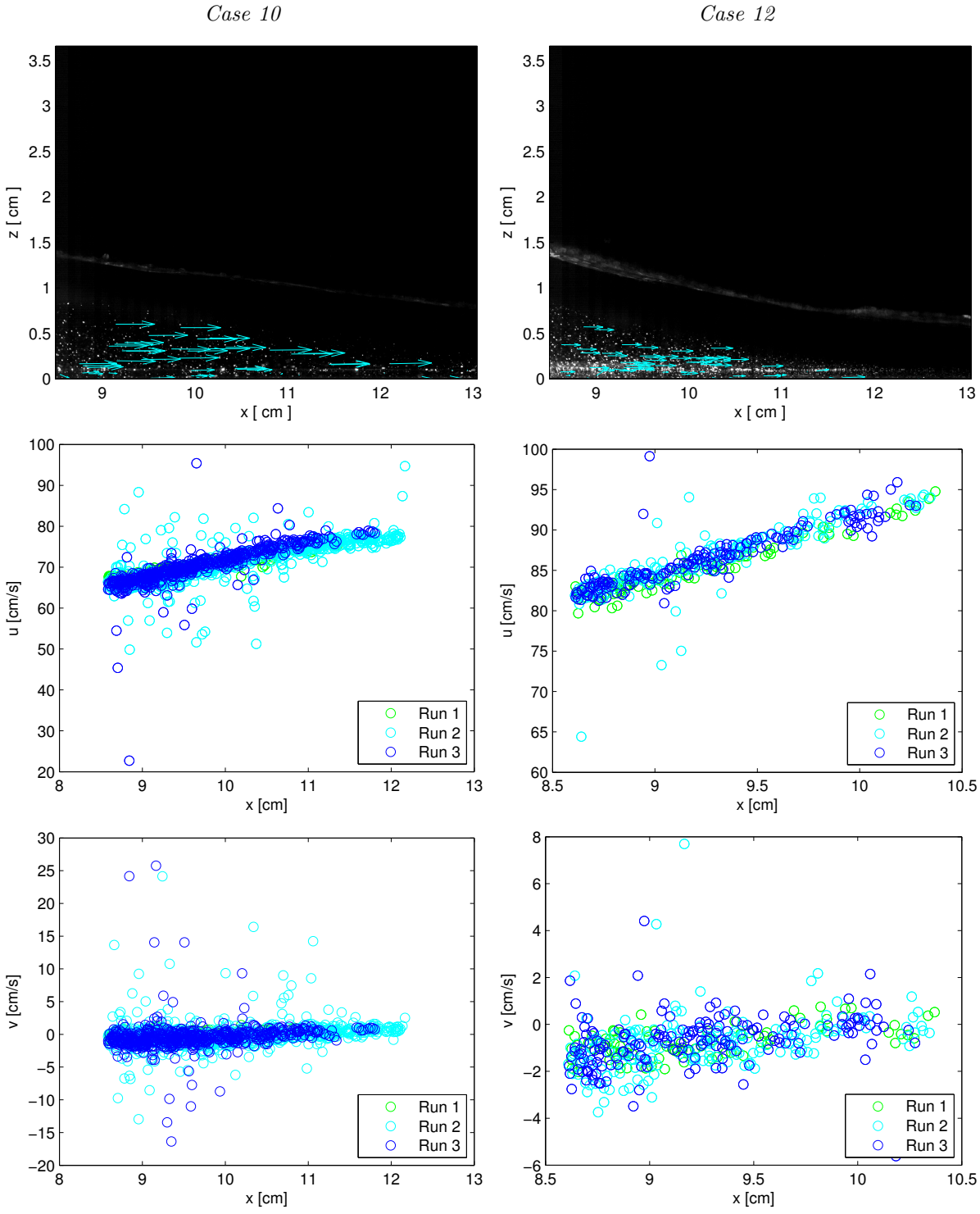

$t_1^{\mathrm{III}} = 7.23s\ z = [0.5 \pm 0.2]cm$ $t_1^{\mathrm{III}} = 7.03s\ z = [0.5 \pm 0.2]cm]$

Figure 5.4: *Top: velocity field, Middle: horizontal velocity, Bottom: vertical velocity*

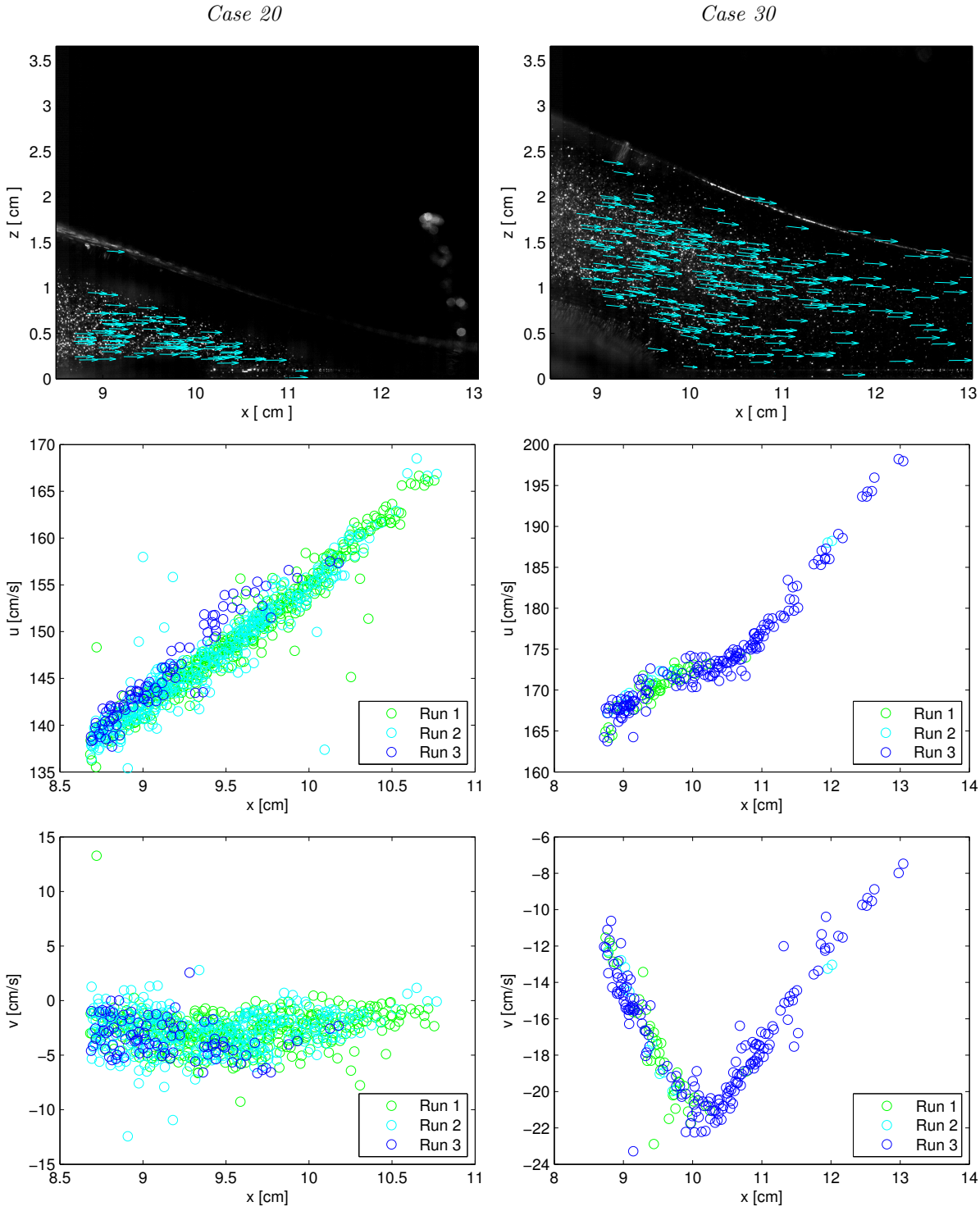

$t_1^{\mathrm{III}} = 6.63s\ z = [0.5 \pm 0.2]cm$ $t_1^{\mathrm{III}} = 6.00s\ z = [1.3 \pm 0.05]cm$

Figure 5.5: *Top: velocity field, Middle: horizontal velocity, Bottom: vertical velocity*

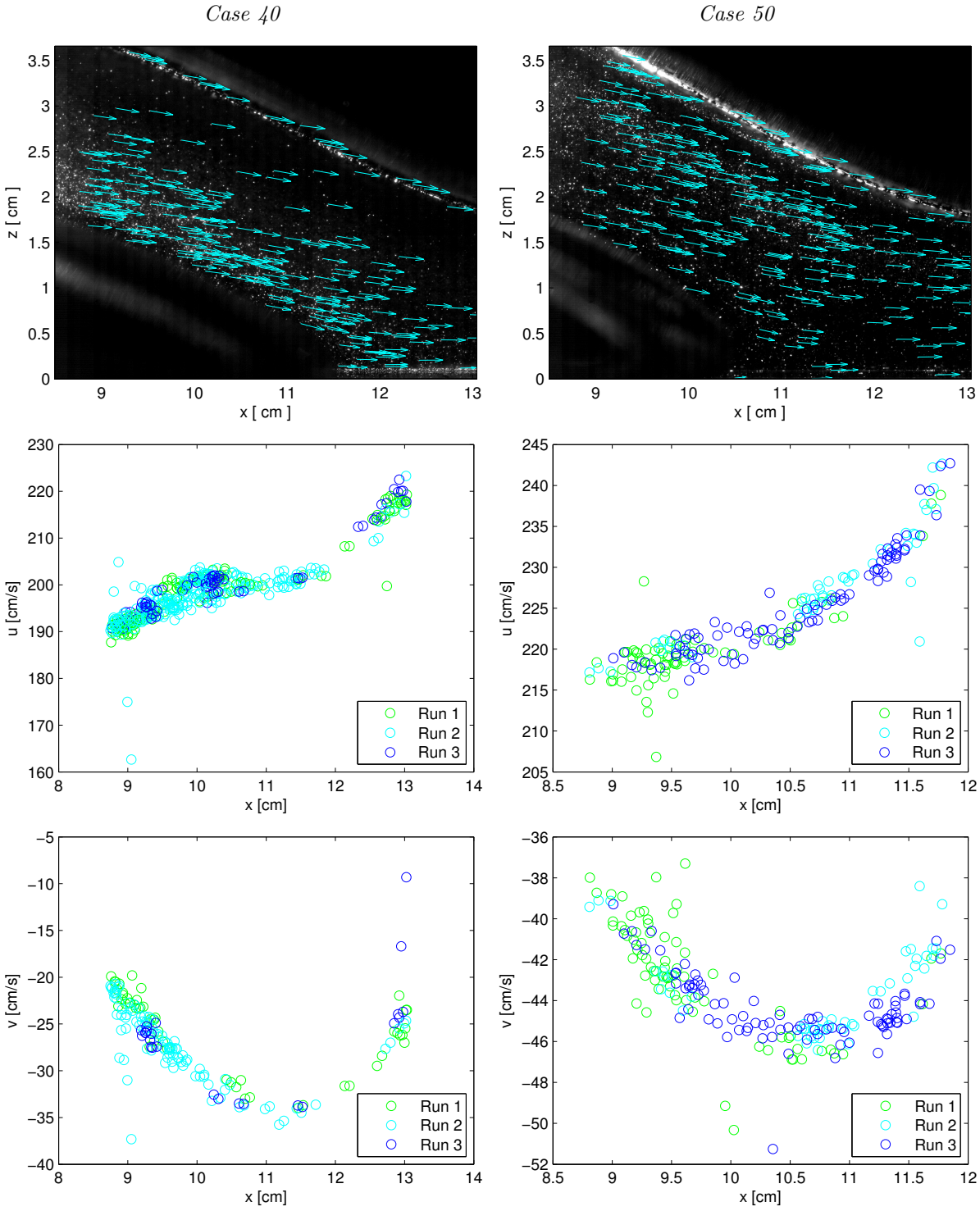

$t_1^{\mathrm{III}} = 5.68s\ z = [1.9 \pm 0.05]cm$ $t_1^{\mathrm{III}} = 5.46s\ z = [2.3 \pm 0.05]cm$

Figure 5.6: *Top: velocity field, Middle: horizontal velocity, Bottom: vertical velocity*

Case:	t_p^{III}	Error	t_1^{III}	$t_1^{\mathrm{III}} - t_p^{\mathrm{III}}$	t_2^{III}	$t_2^{\mathrm{III}} - t_p^{\mathrm{III}}$
	s	%	s	ms	s	ms
10	7.16	0.005	7.23	72.3	7.27	105.7
12	6.98	0.023	7.03	49.3	7.06	82.7
20	6.61	0.010	6.63	24.3	6.66	57.7
30	5.96	0.011	6.00	44.3	6.04	77.7
40	5.62	0.040	5.68	59.7	5.71	93.0
50	5.40	0.100	5.46	61.7	5.50	95.0

Table 5.2: *Times associated with PTV from FOV III. The time t_p corresponds to the time when the plunge enters this FOV*

Table 5.2 shows the times investigated in this section. Including the differences between the arrival of the plunge t_p^{III} and the times of the velocity profiles. $t_1^{\mathrm{III}} - t_p^{\mathrm{III}}$ varies from 24ms to 72.3ms. This implies that t_1 is close to the plunge front. This seems in accordance to the velocity fields shown in Figures 5.4 to 5.6.

Velocity profiles with respect to z are shown in Figure 5.7. The velocity profiles are based on particles located within a vertical strip of 64 pixels (0.12cm). For all cases the horizontal velocities decelerate as a function of time. It seems that velocities are higher for the breaking cases. The velocity profiles show that the velocities are repeatable after the plunge has hit the beach. The boundary layer is well defined for all cases, but seem to increase in size for larger waves. The black graph in figures 5.7(d-f) corresponds to velocities in the fluid above the big air entrapment generated from breaking. These velocities are also repeatable. The maximum velocity is obtained for case 50 where velocities as high as 2.5 m/s are present.

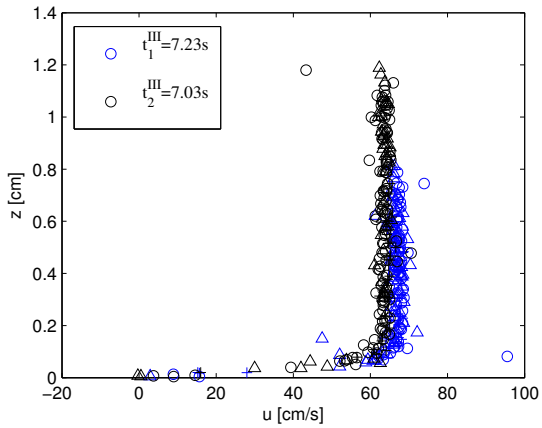

(a) *Case 10:* $x = (9.00 \pm 0.12)cm$

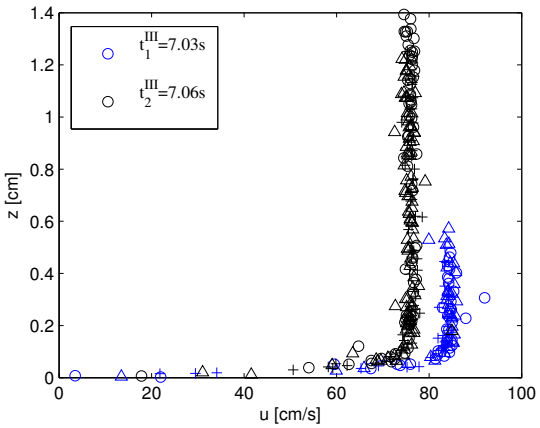

(b) *Case 12:* $x = (9.00 \pm 0.12)cm$

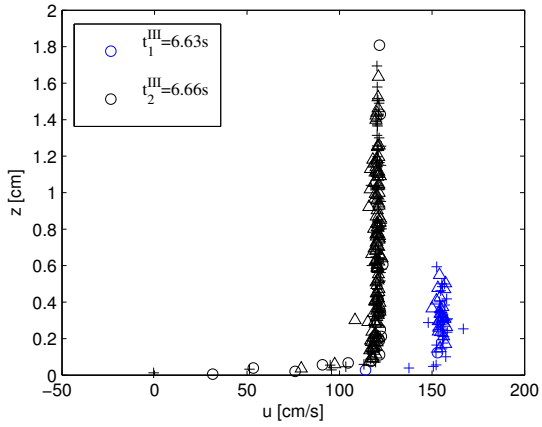

(c) *Case 20:* $x = (10.00 \pm 0.12)cm$

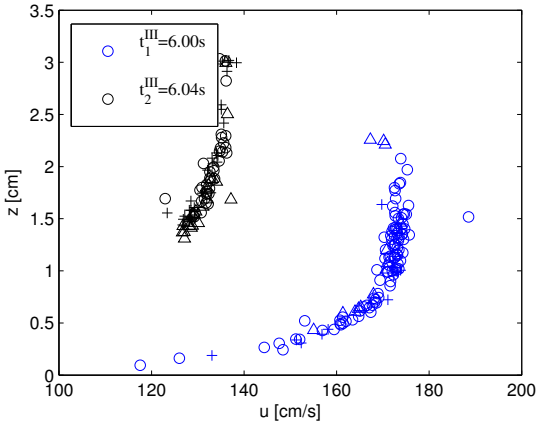

(d) *Case 30:* $x = (10.00 \pm 0.12)cm$

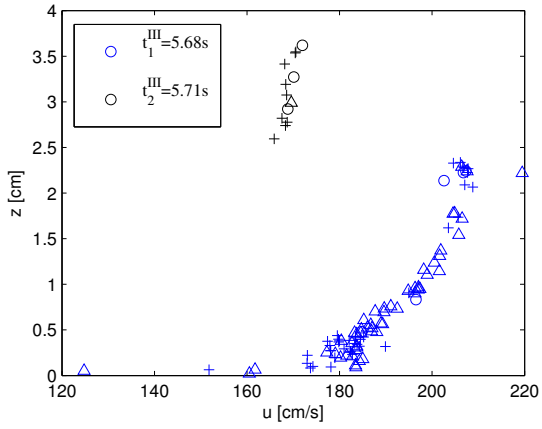

(e) *Case 40:* $x = (12.00 \pm 0.12)cm$

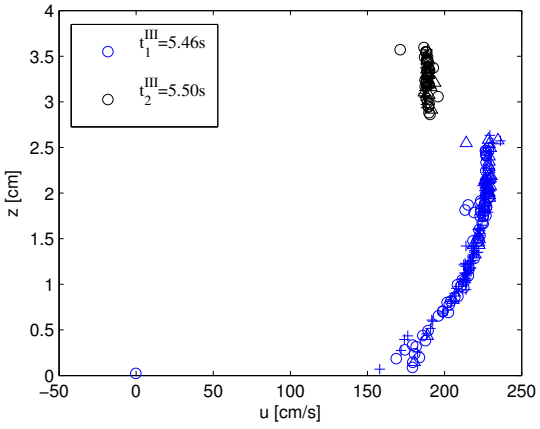

(f) *Case 50:* $x = (11.00 \pm 0.12)cm$

Figure 5.7: *Horizontal velocity profiles, symbols: +, o and △ correspond to run 1,2 and 3.*

5.4 Velocities in the swash zone

In this section results from FOV IV,V and VI will be given. Both PIV and PTV were performed for all FOVs. PTV was performed on early stages, the incoming swash tongue front, whereas PIV was performed on times of flow reversal. Velocities as close to the swash tongue arrival as possible were emphasized for PTV. This resulted in velocity profiles at various times for each case. For all FOVs, times t_1 and t_2 are connected with velocities from PTV. The PIV velocity profiles shown in this section were collected at t_3 and t_4, which correspond to $\pm 0.063s$ before and after flow reversal. As we moved further up the beach to FOV V and FOV VI, the time where the outer flow reverses became harder to determine. This made the times relative to the reversal less accurate for the higher FOVs.

5.4.1 FOV IV

This FOV is located about 40 cm above the still water level along the beach. For the breaking cases 20 - 50 this FOV has problems with air bubbles. The main bubble has not burst, and seeding particles follow small bubbles to the surface. This led to an irregular field of motion. The times t_1^{IV} correspond to velocities as close to the swash tongue front as possible. t_2^{IV} corresponds to velocities as close to front of the main air bubble as possible.

The times when the swash tongue arrives at FOV IV (t_p^{IV}) are given in Table 5.3. They are determined in the same manners as the plunge arrival (Section 5.3). The error is small, which indicates that the run-up is repeatable for this FOV. The times when the main air bubble arrives at this FOV is also given in 5.3. However these times correspond to the first run for each case, since it was problematic to make a generic script that could estimate the time of air bubble arrival.

For all cases the velocities seemed to be repeatable near the swash tongue front (Figure 5.8). An outer constant flow was obtained for all cases, but the size of the boundary layer varied. In addition, the velocities decelerated for all cases. By comparing case 40 and 50 from FOV III, with case 40 and 50 from this FOV, a small increase in velocities can be obtained. This is despite the fact that velocities from FOV III are obtained earlier relative to the arrival of swash tongue.

Case:	t_p^{IV} s	Error %	t_b^{IV} s	t_1^{IV} s	$t_1^{IV} - t_p^{IV}$ ms	t_2^{IV} s	$t_2^{IV} - t_p^{IV}$ ms
10	7.51	0.18		7.63	117.0	7.73	217.0
12	7.26	0.08		7.38	120.3	7.46	200.3
20	6.76	0.01		6.87	106.0	7.07	306.0
30	6.06	0.05	6.18	6.13	58.0	6.16	91.3
40	5.72	0.02	5.80	5.75	67.0	6.77	83.7
50	5.50	0.04	5.58	5.56	65.0	5.58	81.7

Table 5.3: *Times associated with PTV for FOV IV. t_p refer to the arrival of the swash tongue and t_b refers to the main bubble arrival.*

Figure 5.9 shows velocities from PIV. The outer flow seemed to be repeatable for all cases except for case 20, where the outer flow decreased for z=1cm. A visual inspection of the images reveals that this is due to low particle density in a thin strip around this area. For cases 30 - 50 the outer flow seems to be constant for higher values of z than for the lower cases. For cases 10 - 20 the velocities can be divided into three sections, the upper section where $\frac{du}{dz} = 0$, the middle section where $\frac{du}{dz} > 0$ and the section closest to the wall (beach) where $\frac{du}{dz} < 0$. This seemed to be the case for $t = t_3$ and $t = t_4$ for the lower cases 10 - 20. For cases 30 - 50 it seemed that a the section closest to the boundary where $\frac{du}{dz} < 0$ is almost nonexistent for the velocity profiles at $t = t_3$. It seemed that a turbulent and irregular motion was present, but the deceleration of the fluid made it less irregular for the times after the outer flow had reversed. At t_4 the section where $\frac{du}{dz} < 0$ reoccurred.

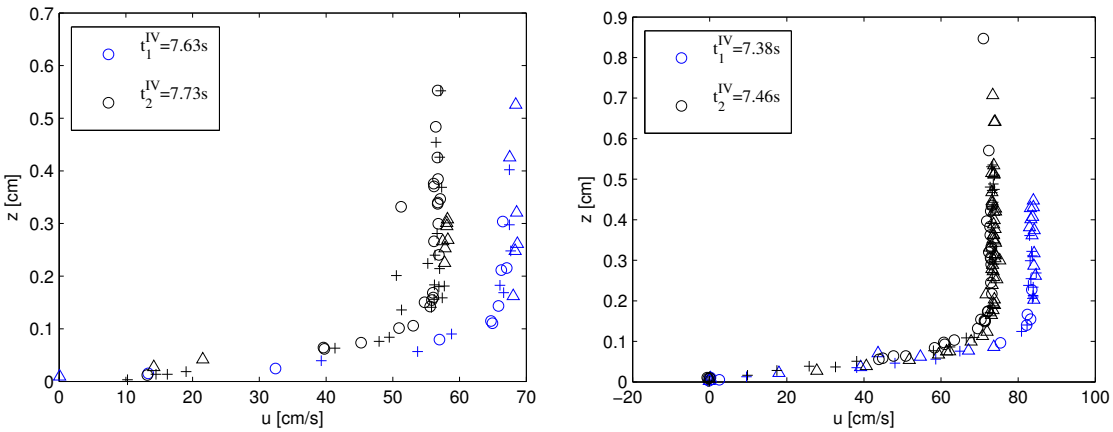

(a) *Case 10*

(b) *Case 12*

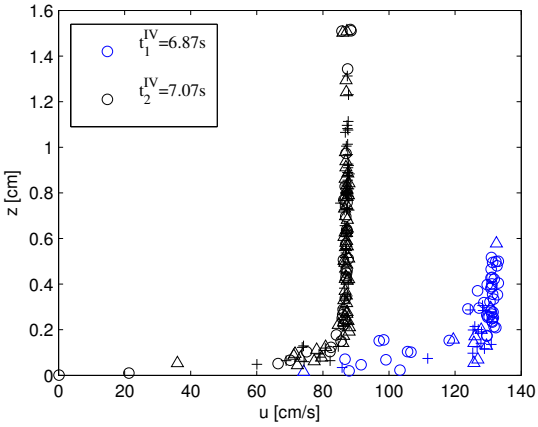

(c) *Case 20*

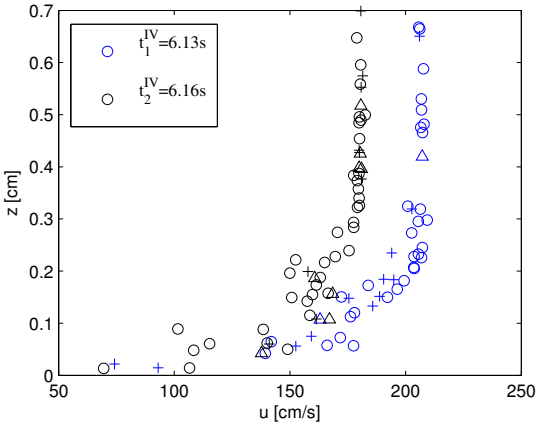

(d) *Case 30*

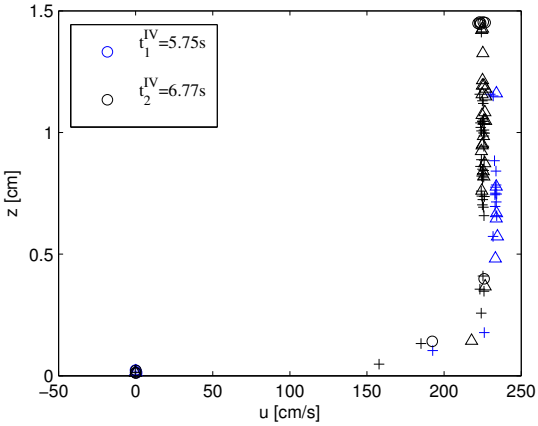

(e) *Case 40*

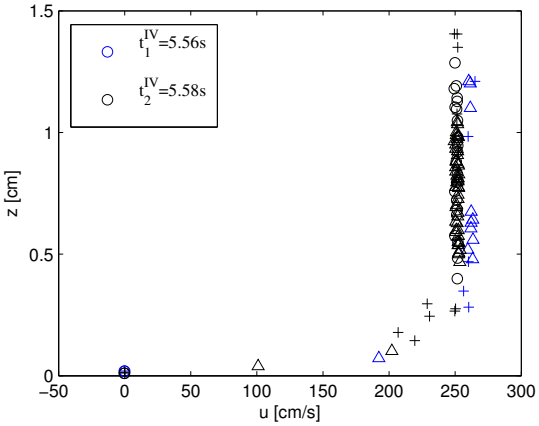

(f) *Case 50*

Figure 5.8: *Horizontal velocity profiles, symbols:* $+$, $\circ$ *and* $\triangle$ *correspond to run 1,2 and 3.* $x = [38.00 \pm 0.12]cm$

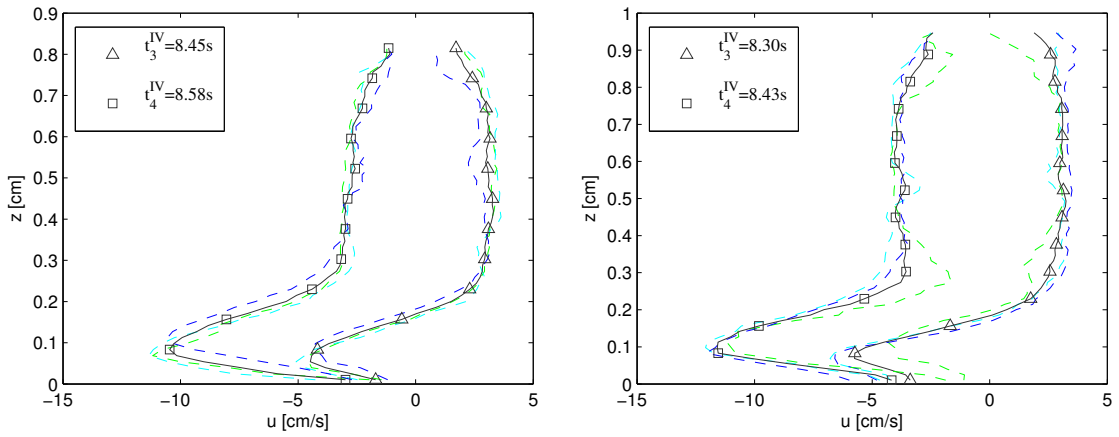

(a) *Case 10*

(b) *Case 12*

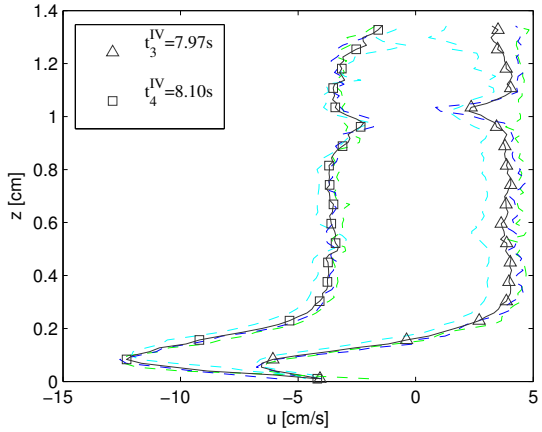

(c) *Case 20*

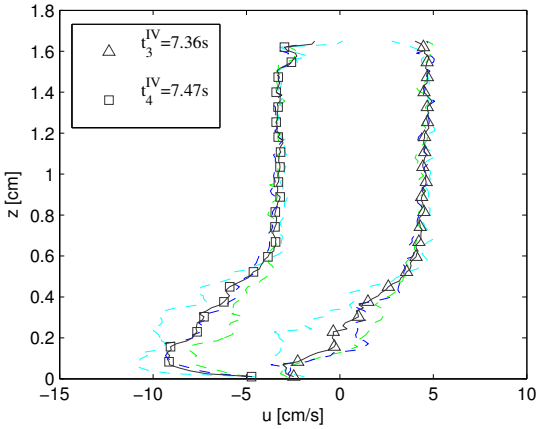

(d) *Case 30*

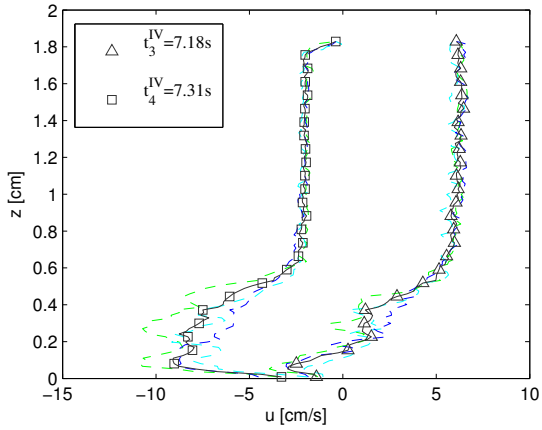

(e) *Case 40*

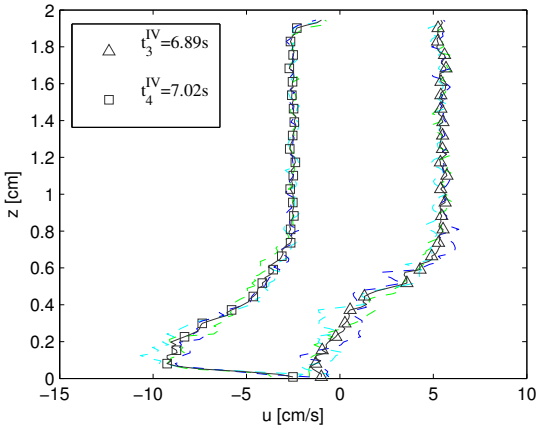

(f) *Case 50*

Figure 5.9: *Horizontal velocity profiles before and after the outer flow reverses. Colors: blue, cyan and green correspond to run 1,2 and 3.* $x = 40.14cm$

5.4.2 FOV V

This FOV is located about 80cm from the still water level. For cases 10 and 12, particles within the swash zone were impossible to detect. Consequently, only cases 20 - 50 will be presented in this section. It was difficult to find particles in the start of the swash tongue for these cases. The times where enough particles were obtained to establish a velocity profile, are given in Table 5.4. It was clear that the times between the swash tongue arrival t_p^{V}, and the first velocity profile t_1^{V},were larger than for the other FOVs. The error in the arrival of the swash tongue was small for all cases, which implies that the run-up was repeatable. At the start of the swash tongue, the surface behaved irregular and the tongue was very thin. The irregular surface was probably due to air bubbles bursting at the surface.

Case:	t_p^{V}	Error	t_1^{V}	$t_1^{\mathrm{V}} - t_p^{\mathrm{V}}$	t_2^{V}	$t_2^{\mathrm{V}} - t_p^{\mathrm{V}}$
	s	%	s	ms	s	ms
20	7.05	0.14	7.49	449.0	7.54	495.7
30	6.28	0.02	6.55	269.7	6.74	463.0
40	5.90	0.08	6.12	230,3	6.23	328.0
50	5.65	0.05	5.73	88.7	5.98	330.3

Table 5.4: *Times associated with PTV for FOV V. t_p refer to the arrival of the swash tongue.*

Figure 5.10 shows the velocity profiles as close to front of the swash tongue as possible. The tongue is about 4mm for case 20, which is really thin. The spread in velocities seemed to be larger for this FOV than for the other FOVs. This could be due to turbulence and irregular motion, but little is known since the number of particles is small. Case also 30 seemed to have a wide spread in velocities, and no constant repeatable outer flow was obtained. The repeatability seemed to increase for increasing case numbers for velocities at t_2^{V}. Case 50 was the only case where enough particles were obtained as early as for the other FOVs. However, the blue graph in figure 5.10 (d) can be compared to the black graph for FOV IV in Figure 5.8 (f), since the times relative to the swash tongue arrival were about the same. The velocities seemed to be in the same range for the two FOVs.

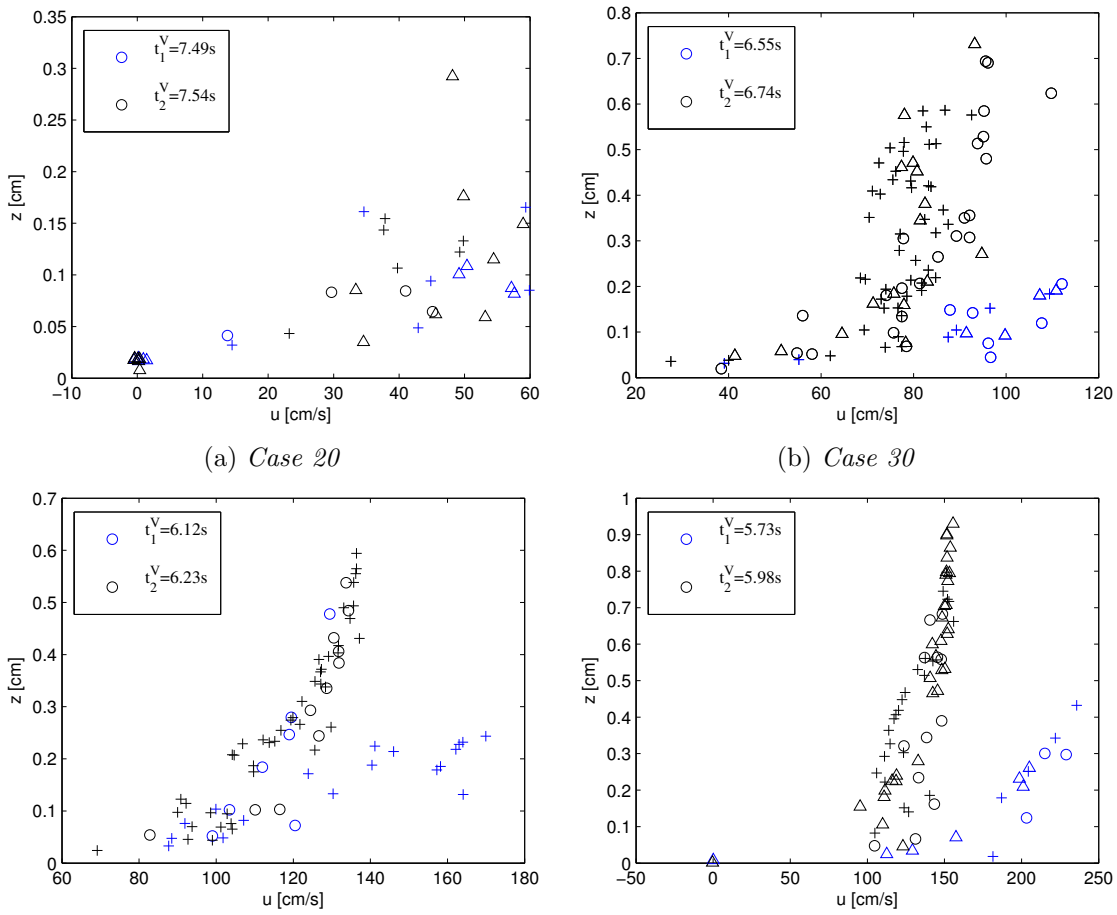

(a) *Case 20* (b) *Case 30*

(c) *Case 40* (d) *Case 50*

Figure 5.10: *Horizontal velocity profiles, symbols: +, ∘ and △ correspond to run 1,2 and 3.* $x = [80.00 \pm 0.12]cm$

None of the cases had an outer flow with constant velocity gradient at times near outer flow reversal (Figure 5.11). This indicates that the flow was more irregular and turbulent than for FOVs closer to the still water level. Since there is no clear defined outer region, the time of reversal was estimated only by visual inspection, resulting in a small relative time error. The cases seemed to be less repeatable for this FOV, than for FOV III and IV.

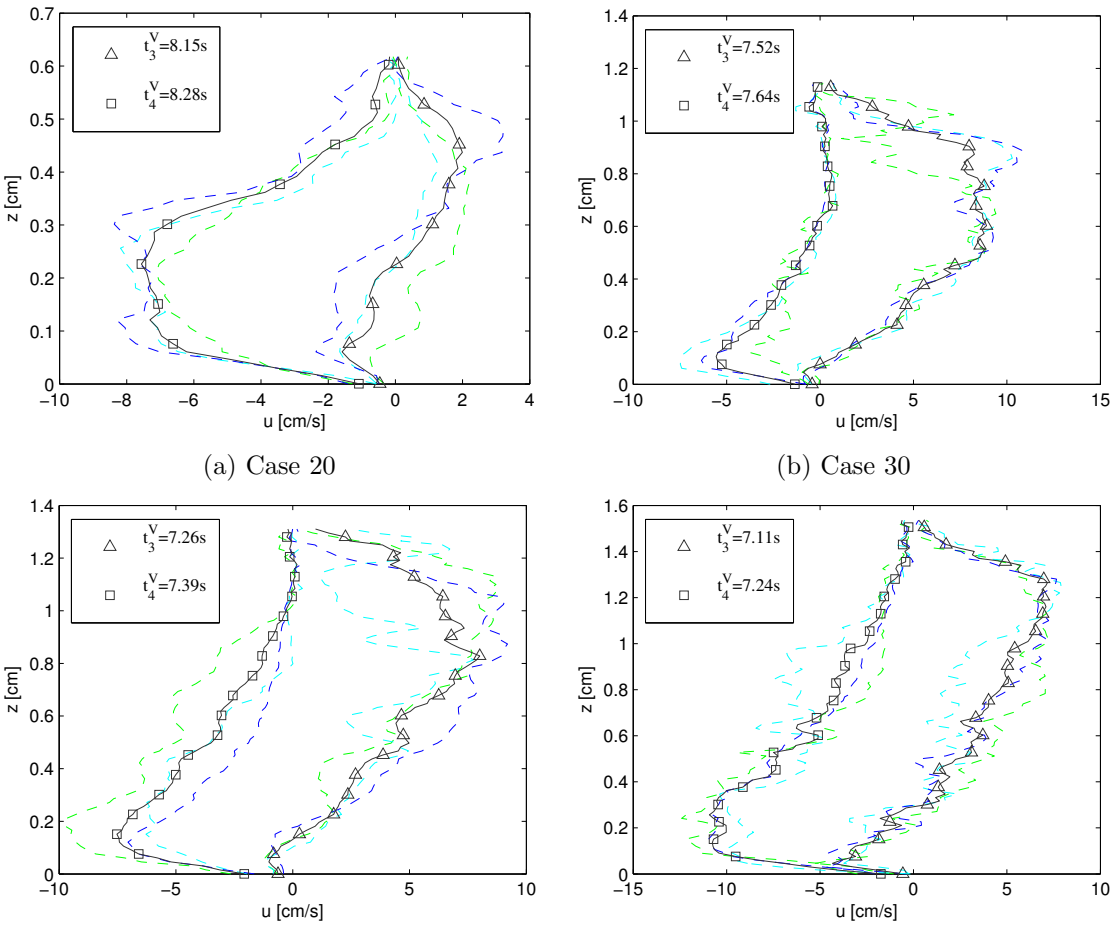

(a) Case 20

(b) Case 30

(c) Case 40

(d) Case 50

Figure 5.11: *Horizontal velocity profiles before and after the outer flow reverses. Colors: blue, cyan and green correspond to run 1,2 and 3.* $x = 81.40cm$

5.4.3 FOV VI

This FOV is located about 120cm from where the still water reaches the beach. In this section, only cases 30, 40 and 50 will be presented. The swash tongue was too thin for particle detection for the other cases. It was however easier to find particles for the cases 30 - 50 at this FOV, than at FOV IV. I believe that this is because the surface has calmed down, after the bubble bursting. This results in earlier velocity profiles relative to the swash tongue arrival for this FOV, than for FOV V (Tables 5.4 and 5.5).

Case:	t_p^{VI}	Error	t_1^{VI}	$t_1^{VI} - t_p^{VI}$	t_2^{VI}	$t_2^{VI} - t_p^{VI}$
	s	%	s	ms	s	ms
30	6.55	0.15	6.82	270.3	7.04	497.0
40	6.10	0.08	6.14	48.0	6.60	511.3
50	5.32	0.10	5.88	62.3	6.33	515.7

Table 5.5: *Times associated with PTV for FOV VI.* t_p *refer to the arrival of the swash tongue.*

Figure 5.12 shows the velocities obtained as close to the front of the swash tongue as possible. In the front of the tongue, the velocities seemed to be more spread than for the other FOVs (blue graph) at t_1. Overall, the spread in velocities close to the swash tongue seem to increase as we move upwards the beach.

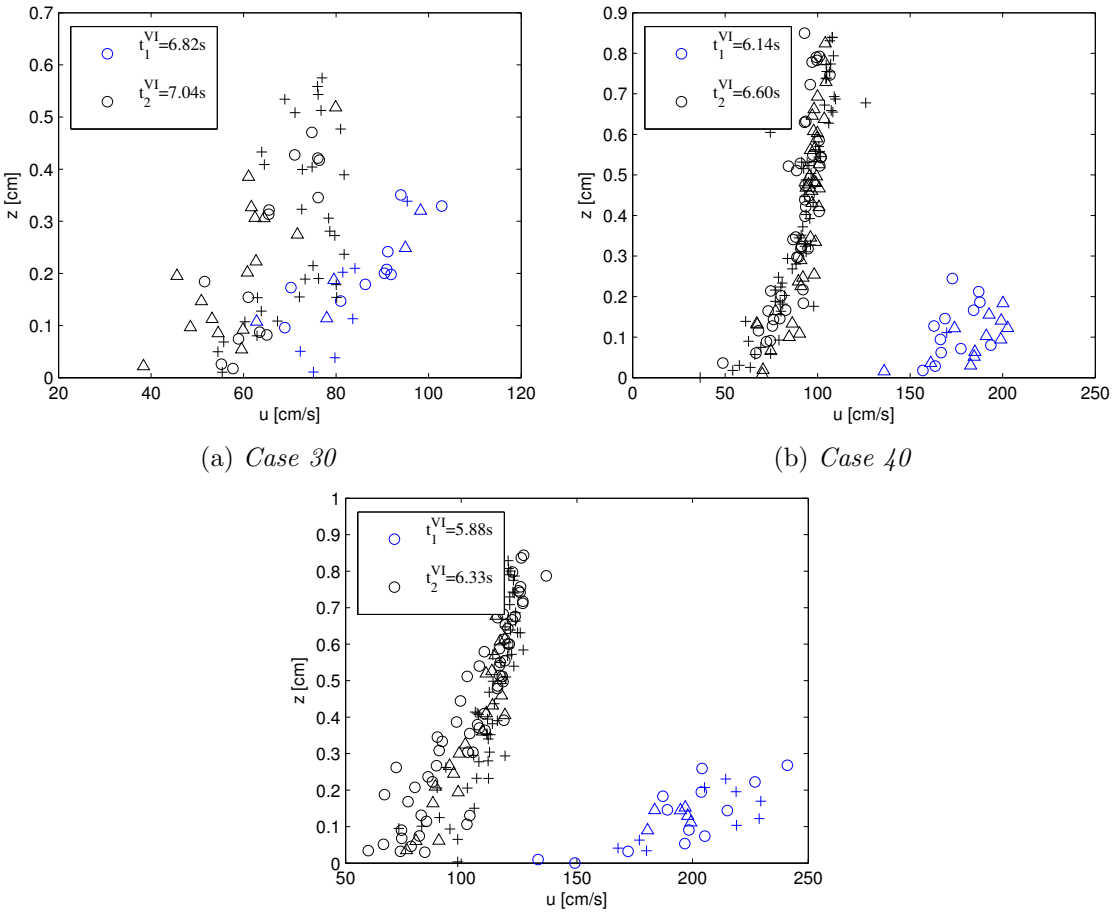

(a) *Case 30* (b) *Case 40*

(c) *Case 50*

Figure 5.12: *Horizontal velocity profiles, symbols:* $+$, $\circ$ *and* $\triangle$ *correspond to run 1,2 and 3.* $x = [120.00 \pm 0.12]cm$

Velocities before and after reversal of the flow, are given in Figure 5.13. The repeatability was not as good for this FOV as for the other FOVs. The velocity profiles seemed to be more turbulent than for the earlier FOVs. Especially for case 50, where the velocity profile at $t = t_3^{\mathrm{VI}}$, seemed similar to the velocities profiles from turbulent channel flow. Overall, the velocities before and after flow reversal, seemed to become more turbulent as we move further up the beach.

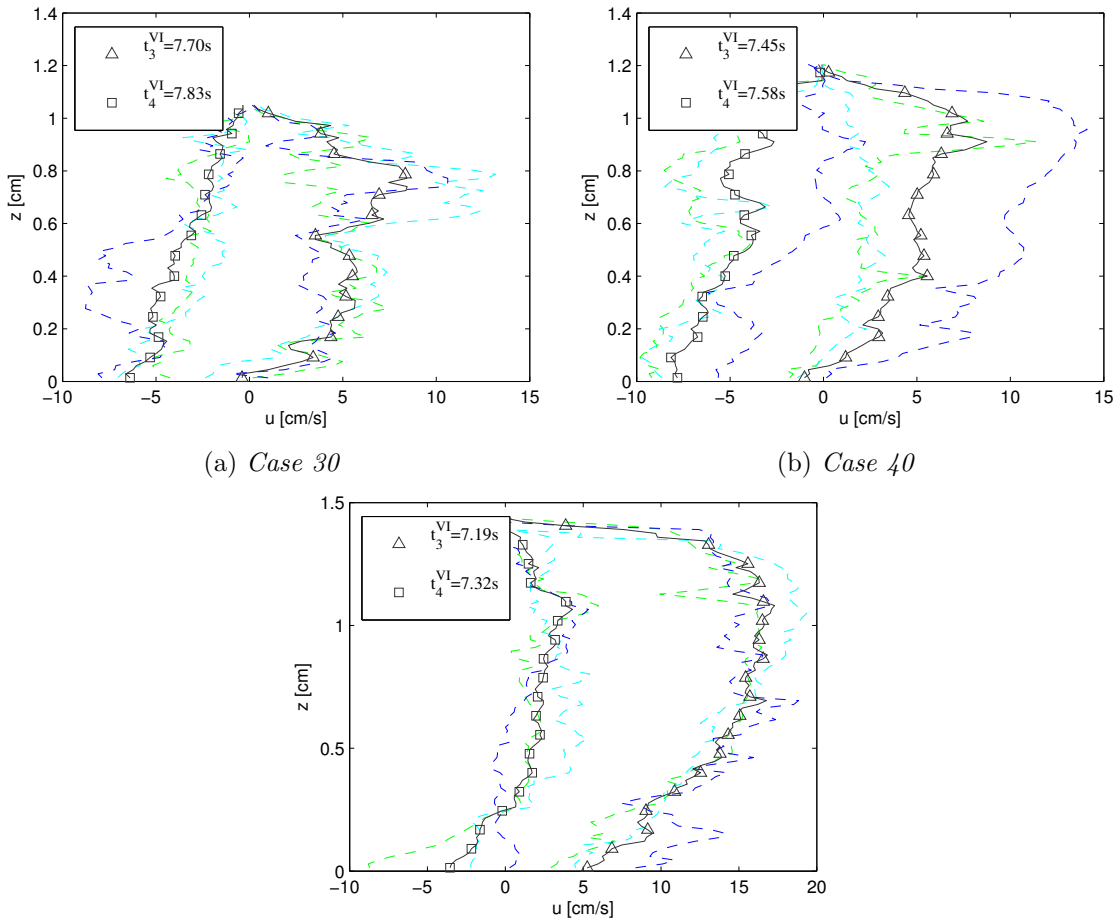

(a) *Case 30*

(b) *Case 40*

(c) *Case 50*

Figure 5.13: *Horizontal velocity profiles before and after the outer flow reverses. Colors: blue, cyan and green correspond to run 1,2 and 3.* $x = 121.25cm$

Visual inspection of movies of this FOV shows that a systematic rolling effects were present for some of the cases for a short period of time. It looks like particles follow a rolling trajectory (cycloid). Figure 5.14 shows how horizontal velocities vary at one spot in fluid as a function of time. The velocities seems to oscillate, in addition to a linear decaying trend. I believe that this is due to some rolling effects. Further investigation is needed to determine what causes this effect.

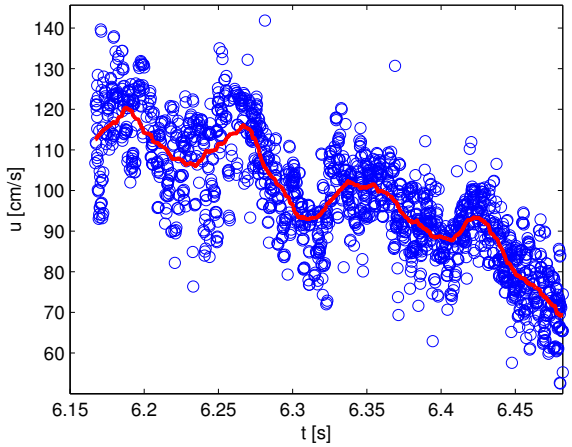

Figure 5.14: *Collection of velocities of particles whithin a distance of 0.05cm from the point(x,z)=(120,0.3)cm. The data is collected from Case 50, run 2.*

5.5 Maximum run-up

In this section results from experiments where the camera is mounted above the beach is given. The maximum run-up was found by checking images pixel by pixel, and searching for areas where the total intensity were larger than some threshold. The code is scripted in MATLAB and a visual inspection was performed to validate the results. The results and errors are given in Table 5.6. The maximum run-up seemed to be repeatable in both time and space. An image of the maximum run-up for case 10 is shown in 5.15.

	Max runup	**Max error**	**Time**	**Error in time**
Case 10	87.25 cm	1.68 %	8.86 s	0.15 %
Case 12	105. 67 cm	0.27 %	8.67 s	0.15 %
Case 20	147.37 cm	0.93 %	8.53 s	0.31 %
Case 30	191.67 cm	1.08 %	8.03 s	0.78 %
Case 40	227.42 cm	0.11 %	7.82 s	0 %
Case 50	267.46 cm	2.27 %	7.30 s	1.64 %

Table 5.6: *Maximum runup*

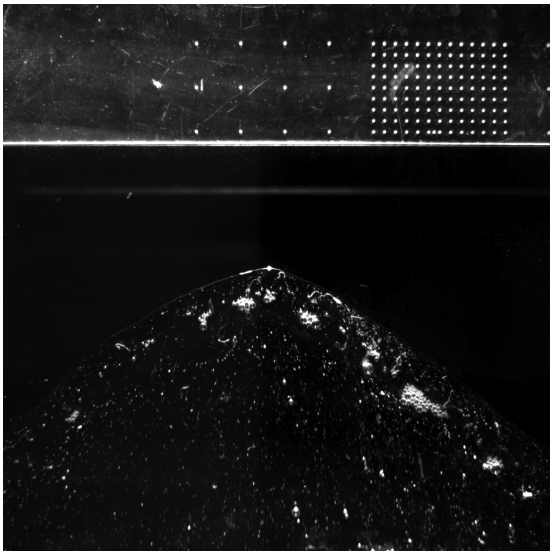

Figure 5.15: *Image from case 10, run 2, $t = 8.87s$. The upper part of the picture shows the coordinate sheet.*

The shape of the shoreline seemed to vary a lot for the breaking cases. A comparison of the shapes from different runs is shown in Figure 5.16. The shape seemed to be repeatable for case 10, but the variation across the beach was large. The maximum seemed to vary with about 10cm for this field of view. If this trend was present throughout the entire cross section of the beach, measurements from different values of y will estimate different maximum run-ups. This is probably due to the bending of the beach, documented in Section 4.2. The variation of 3mm in the z direction should correspond to 3cm in the x direction since the beach inclination is 1:10. It is clear from figure 5.16 that the bending has a larger impact on the run-up than a 3cm variation. The effect of the bending might therefore play a central role in measurements of maximum run-up. This effect will also occur for the breaking cases and will be discussed further in the next section.

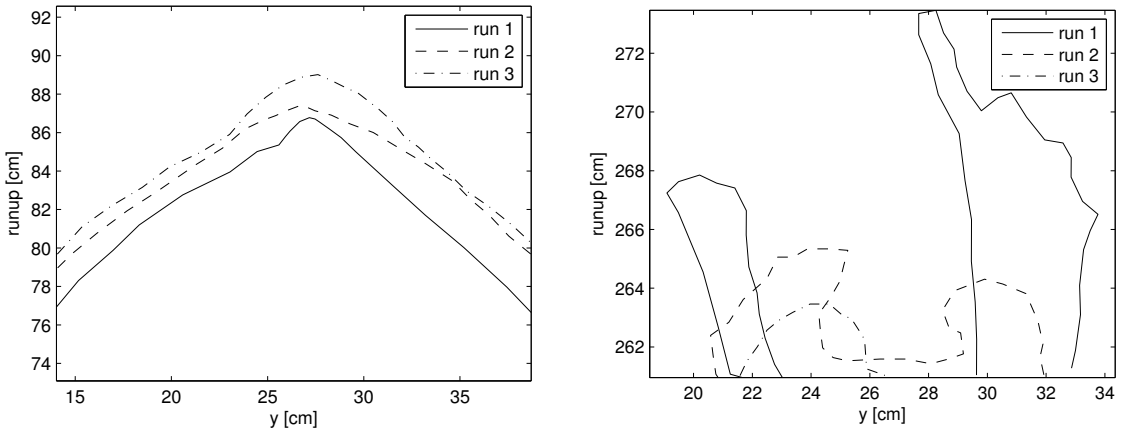

(a) *Case 10* (b) *Case 50*

Figure 5.16: *Shoreline profiles at max run-up.*

5.6 Surface profiles of the run-up

In this section results from FOV A and FOV B will be given. A selection of cases 10, 30 and 50 will be shown. The surface profiles were tracked manually for each case and each run, since a general script was difficult to create due to air bubbles near the surface. An image from the experiments is given in Figure 5.17.

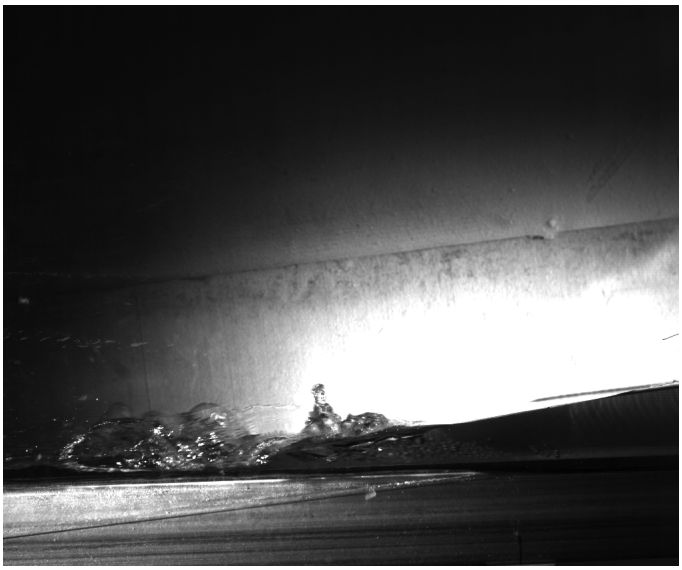

Figure 5.17: *Image from FOV A, for case 50 run 1, at t=5.65s*

The surface profile for case 10 is shown in figure 5.18. The first two surface profiles t_1 and t_2 correspond to times associated with plunge and swash tongue arrival for FOV *III* and FOV *IV*. The last profile t_3 corresponds to times of maximum run-up.

Figure 5.18 shows that run-up is in agreement with experiments from FOV III and FOV IV. The run-up reached about 35cm at t_p^{IV}, which is about 1cm from where FOV IV starts. As mentioned in the previous section, the surface profiles are not in agreement with measurements from maximum run-up for case 10. There seems to be about 22cm difference between the measurements. The real maximum run-up is measured to be located about y=26cm (Figure 5.16a), whereas the run-up investigated in this section corresponds to a strip around y=7.5cm, where y corresponds to the distance from the wall in the wave tank. A difference of 22cm seems reasonable if the shoreline varies as shown in Figure 5.16a. The surface profiles seem to be repeatable for case 10.

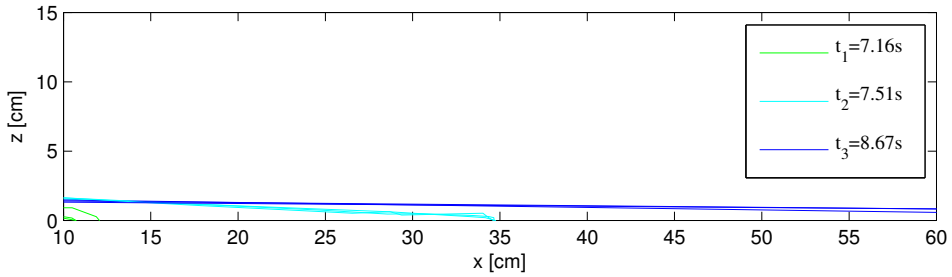

(a) *FOV A*

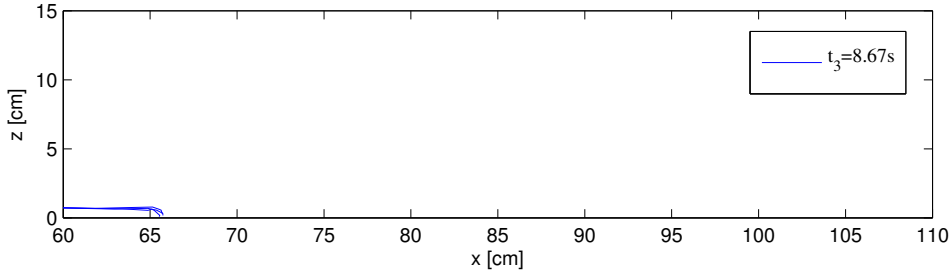

(b) *FOV B*

Figure 5.18: *Surface profiles for case 10. Three repetitions are plotted.*

It was hard to track the surfaces for the breaking cases 30 and 50, since they were unstable due to air bubble bursting. The results are shown in Figure 5.19 and 5.20. The times t_1, t_2 and t_3 are associated with plunge and swash tongue arrival from FOV III and FOV V and maximum run-up.

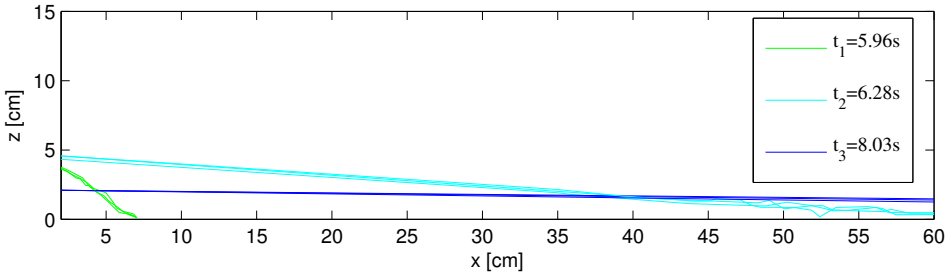

(a) *FOV A*

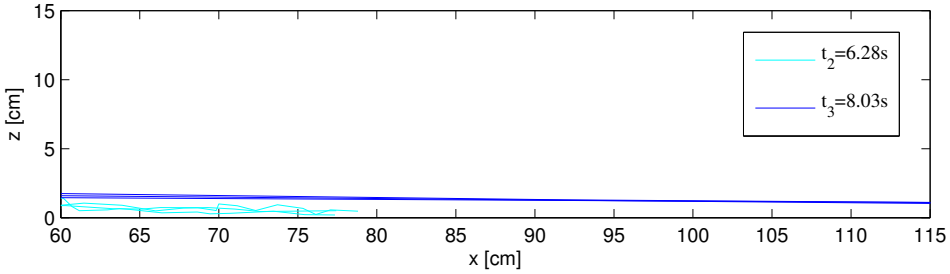

(b) *FOV B*

Figure 5.19: *Surface profiles for case 30. Three repetitions are plotted.*

For t_2, the surface was unstable and not repeatable for cases 30 and 50 (Figures 5.19 and 5.20). There was a differences from measurement at FOV *V* for these two cases. I believe this is due to inaccuracy in the tracking process of the surface profiles. It was extremely difficult to track the surface when air bubbles were present. This can be related to the difficulties of finding particles close to swash tongue for FOV V. The surface becomes steady again when all the air is separated from the water. This makes it easier to track the surface again at t_3.

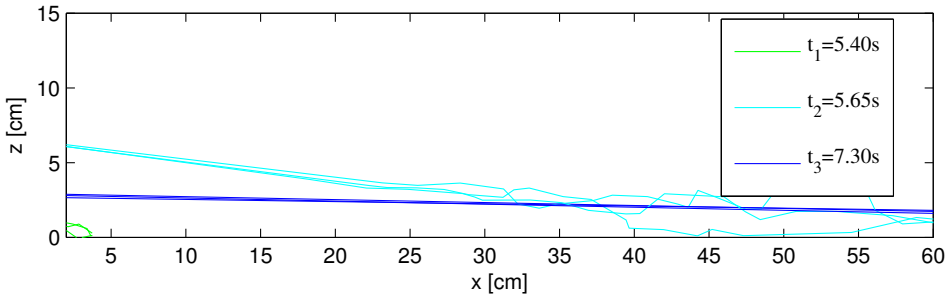

(a) *FOV A*

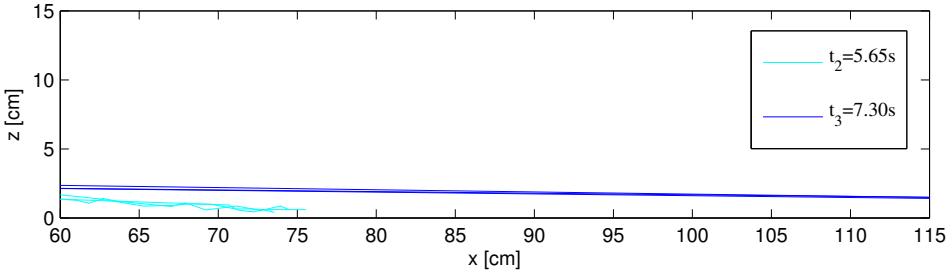

(b) *FOV B*

Figure 5.20: *Surface profiles for case 50. Three repetitions are plotted.*

Chapter 6

Conclusion

In this thesis, velocities in plunging breakers in the swash zone and at the plunge point have been investigated. Six different solitary waves were generated from non-breaking to breaking cases. PIV and PTV were performed on images captured from six different FOVs. The FOVs were located from [-10 to 120]cm from where the still water level intersected with the beach. The post processing was mainly done in DigiFlow. High resolution velocity measurements close to beach were conducted. Velocity profiles with respect to z were given for the swash zone. At the plunge point velocity profiles with respect to both x and z were shown.

Surface elevation was measured with ultrasonic gauges for all cases. The maximum run-up was investigated for all cases, and shoreline profiles for case 10 and 50 have been shown. Surface profiles of the run-up have been studied on a large scale. Aspects regarding the properties of the beach and the fluid have been documented and discussed. Overall, a large range of measuring methods were used to acquire a comprehensive overview of field. In the following section I will present a brief summary of the results, before giving my suggestions for future work.

6.1 Concluding remarks

- Surface elevation of the incoming waves coincided with theory from Tanaka (1986) and Fenton (1972).
- The effect of the joint between the PETG plates seemed to be minimized by removing extra silicone from the joints. This improved the measurements of the boundary layer.
- Stagnation flow was observed when the plunge hit the beach. Ap-

plication of this can be related to loads on offshore structures due to being hit by a plunging breakers. At the stagnation point the velocity will be at a minimum. From Bernoullis equation the pressure will be highest at this point. This results in a maximum force on the bodies at this point.

- The highest velocities obtained was about 2.5m/s. This seemed to be the same magnitude as in Kikkerta et al. (2011).
- As we moved further up the beach, the turbulence seemed to increase and the repeatability of velocity profiles seemed to decrease.
- There was a slight tendency that turbulence effects seemed to be larger for up-rush than for backwash, this seemed to be in agreement with results from Cowen et al. (2003) and Barnes et al. (2009), but in contradiction to Kikkerta et al. (2011).
- There seemed to exist some rolling effects in the front of the swash zone. This needs to be further investigated.
- Maximum run-up seemed to be repeatable, but large differences in the maximum run-up cross shore profiles were obtained due to bending of the beach.

To sum up, the experiments showed new aspect of wave breaking, and revealed that more work is needed in this field.

6.2 Future perspectives

PIV and PTV could be performed further up the beach than FOV VI. A difficulty regarding this FOV was focusing the camera, which is discussed in section 4.5. To investigate velocities further up the beach, I would recommend making a removable dam, such that water could be dammed in front of the FOV. Then the focusing of the camera could easily be done on arbitrary location on the beach. Since the problems with air bubbles only was relevant for the FOVs closer to the still water level, I will assume that good quality measurements could be provided for locations further up the beach than FOV VI.

The non-breaking cases 10 and 12 could be compared with a boundary integral model. If the case 10 and 12 coincides with the model, it will increase the credibility of the measurements. The breaking cases 20 - 50 could be compared with a RANS model, as done in Rivillas-Ospina

et al. (2012).

Further investigation is needed especially in the areas where the particles seem to roll inside the swash tongue. This effect can easily be detected in movies, but needs further investigation to be documented. Analysis of the bed shear stress could be performed. The bed shear stress could be calculated from the horizontal velocity gradient close to the wall.

The quality of the surface profile measurements of the run-up were not as good as expected. The choice of focal lens and size of the field of view can be optimized. The large field of view provided images with poor resolution, which resulted in low accuracy in the measurement. The camera should be placed closer to the wave tank and multiple field of views should be introduced.

A more detailed description of the turbulence could be observed if more repetitions had been made for each case, such that an ensemble average could be used. Then fluctuating velocities and turbulent kinetic energy could be provided.

Appendices

Appendix A

Shear stress measurements

The main goal of the shear stress measurements is to verify the PIV and PTV measurements from the swash zone of breaking waves. We want the shear stress measurements to imply the same result as PIV and PTV presents. Shear stresses will be measured with Measurement science enterprise's MicroS systems (science enterprise Inc, 2014). Before mounting the the shear stress sensor into the wave tank, the sensor should be validated against theory. The shear stress probe will therefore be mounted into a horizontal pipe, where theory is well established.

A.1 Pipe flow

There are several flow regimes for horizontal one phase pipe flow, depending on the Reynolds number. Reynolds number is defined as the ratio between inertial forces and viscous forces for pipe flow. It is given by:

$$Re = \frac{\rho U D}{\mu} \tag{A.1}$$

, where D is the diameter of the pipe, U is the mean velocity, μ and ρ are the dynamic viscosity and density of the fluid. For Reynolds numbers lower than 2000, the flow is considered to be laminar. For Reynolds numbers above 3000 the flow is considered to be fully developed turbulent.

A.1.1 Laminar pipe flow, Hagen-Poiseuille Flow

Hagen (1939) and Poiseuille (1840) (*Viscous fluid flow*, 2006) were the first to find an analytic solution to Navier Stokes equations for laminar pipe flow. Consider a horizontal pipe with radius r_0, let the x-y plane

be the cross section of the pipe, and let the z axis be parallel to the pipe length (see figure A.1).

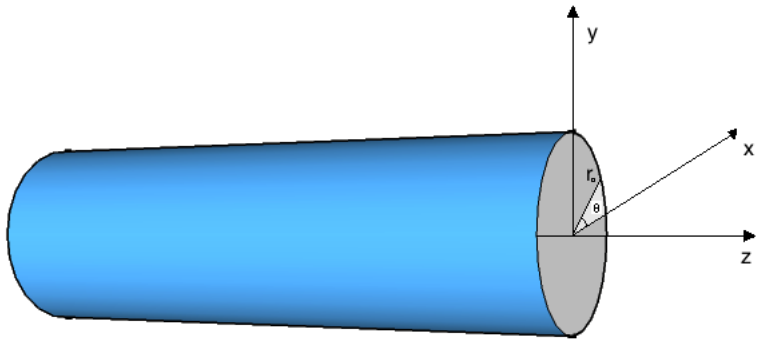

Figure A.1: *Pipe flow*

Introduce polar coordinates, and assume the horizontal velocity to only be dependent on the distance from origo r, $\mathbf{u} = \{0, 0, u(r)\}$. Then the Navier Stokes equation in z-direction becomes

$$\nu \frac{1}{r}\frac{\partial}{\partial r}\Big(r\frac{\partial}{\partial r}u(r)\Big) = \frac{1}{\rho}\frac{\partial p}{\partial z}. \tag{A.2}$$

Derivation of the r and θ momentum equations shows that $\frac{\partial p}{\partial z}$ must be constant. Integration of equation A.2, and insertion of no slip boundary conditions gives the solution:

$$u(r) = \frac{1}{4\mu}\frac{\partial p}{\partial z}\Big(r^2 - r_0^2\Big) \tag{A.3}$$

The wall shear stress is defined as

$$\tau_w = \mu\Big(-\frac{du(r)}{dr}\Big)_w = \frac{1}{2}r_0\Big(-\frac{dp}{dz}\Big) = \frac{4\mu\overline{u}}{r_0} \tag{A.4}$$

, where $\overline{u}$ corresponds to the mean velocity. The last part of equation A.4 is a substitution of the pressure drop. The pressure drop is calculated from the volumetric flow rate Q.

A.1.2 Friction factors and estimates on wall shear stresses in turbulent pipe flow

The wall shear stress is non dimentionalized by the dynamic pressure $\rho\overline{u}^2$. There are two friction factors used today for pipe flow. The *Darcy friction factor* and the *Skin friction factor*:

$$\begin{aligned} \lambda &= \frac{8\tau_w}{\rho\overline{u}^2} \\ C_f &= \frac{2\tau_w}{\rho\overline{u}^2} \end{aligned} \tag{A.5}$$

The mean velocity can be found analytically from Hagen-Poiseuille solution, and a connection between the friction factors and Reynolds number is given by A.6.

$$\begin{aligned} \lambda &= \frac{64}{Re} \\ C_f &= \frac{16}{Re} \end{aligned} \tag{A.6}$$

The relations above are only applicable for laminar flow. The friction factors for turbulent flow have been estimated by H. Blasius (1913). From dimensional analysis he found an estimate for the *skin friction factor* $C_f \approx \frac{0.0791}{Re^{1/4}}$. An improvement of Blasius approximation, where the roughness of the pipe is taken into consideration, has been done by Moody (1944) (Figure A.2). Colebrook (1939). found an implicit formula given by:

$$\frac{1}{\sqrt{\lambda}} = -2log_{10}\Big(\frac{\epsilon}{3.7D} + \frac{2.51}{Re\sqrt{\lambda}}\Big) \tag{A.7}$$

,where ϵ is the pipe roughness, and Blasius solution is given as an initial guess.

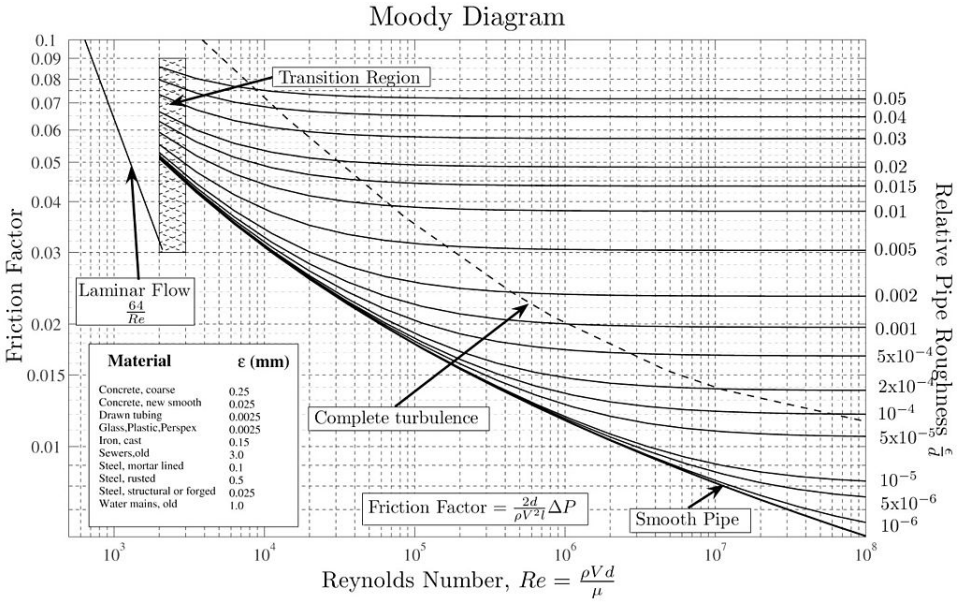

Figure A.2: *Friction factor as a function of Reynolds number and roughness. The figure was created by Beck and Collins (2008)*

Direct numerical simulation of pipe flow with Reynolds number 44k was done by Wu and Moin (2008). A second order finite difference method was used and the Navier Stokes equations were solved for 630 million grid points. The bed shear stress can be calculated from this solution.

A.2 MicroS systems

MicroS shear stress sensor measures velocity gradients close to walls. The instrument is based on the same principles as Laser Doppler Velocimetry (LDV) and an introduction is given in science enterprise Inc (2014). The sensor can measure velocity gradients in a region very close to the wall, and the wall shear stress can therefore be calculated directly from the velocity gradient measured.

In all wall bounded flows there exists a linear sub-layer (Universal equilibrium layer), where the velocities are linearly dependent on the distance from the wall (see equation A.8),

$$u = Cy \tag{A.8}$$

where C is a constant. MicroS shear stress sensor must be calibrated against this constant. The sensor can detach particles within a distance

of 75μm from the wall. In this region, the velocity gradient measured corresponds to the velocity gradient at the wall. The wall shear stresses can therefore be calculated by:

$$\tau_w = \mu\Big(\frac{\partial u}{\partial y}\Big)_w \tag{A.9}$$

The MicroS sensor generates a linear diverging fringe pattern. The distance between two fringes δ can be found by multiplying the distance from the wall y, and the slope of the first non-vertical fringe k, $\delta = ky$. When particles pass through the fringes at a distance y from the wall, they reflect laser light with a different frequency than the initial frequency. This frequency will be proportional to the particle velocity u and inversely proportional to the distance between the fringes δ.

$$f = \frac{u}{\delta} = \frac{Cy}{ky} = \frac{1}{\mu k}\tau_w \tag{A.10}$$

The laser signals are controlled by a hardware box, which contains electronic drivers, band pass filter and burst processor acquisition hardware. The box is connected to a computer where software is installed to control the hardware.

A.2.1 Probe details

Details concerning the components in the MicroS sensor are available in Modarress et al. (2000). The instrument contains a diode laser source, two optical elements (DOE), a 700 μm layer of fused silica, a thin chrome layer, and a detector. A diverging beam of laser light is sent from a diode laser towards an optic element (DOE). The optical element focuses the beam such as when the light has travelled through the fused silica, the beam is focused into two line foci. These foci correspond to two slits in the chrome layer. The slits are 2μm wide and are separated with a distance of 10μm. The laser light becomes a fringe fan when it enters the fluid flow. Particles that pass the fringe fan reflect the light. The reflected light has a different frequency then the frequency initially set. See equation A.10. The reflected light hits a large window of 100μm in the chrome layer and the light spreads through the fused silica again. At the end of the silica the light hits another optical element which focuses the light into the detector.

A.3 Experimental set-up

Experiments were carried out in the hydrodynamic lab at UiO. A 25m perspex pipe with 5cm diameter was filled with water. The fluid was

seeded with polyamid particles with a diameter of 10μm from *Dantec dynamics*. The flow rate was controlled by a pump, and experiments were carried out with different flow rates.

Pump frequency $[kHz]$	20	30	35	40	45	50
Mass flow rate $[kg/s]$	1.54	2.35	2.75	3.20	3.63	4.06

Table A.1: *Flow rates*

The mass flow rates were measured by a Coriolis flow meter and the connection between flow rates and pump frequency is given in table A.1 To get the same amount of samples for each flow rate, the measuring time had to be altered. Parameters from one experiment are given in table A.2 and the results are shown in the next section. The flow was fully turbulent for all cases.

Parameter	Value
Calibration constant	61.8
Fluid Viscosity	$9.32 \cdot 10^{-4}$
Threshold	8300
Decimation factor	1
FFT points	1024
Threshold	1
Min stress	-500Pa
Max stress	1000Pa

Table A.2: *Experimental parameters*

A.4 Results

The raw data from the experiment with parameters as in Table A.2 is shown in Figure A.3. There are a lot of measurements where the shear stress is equal to zero.

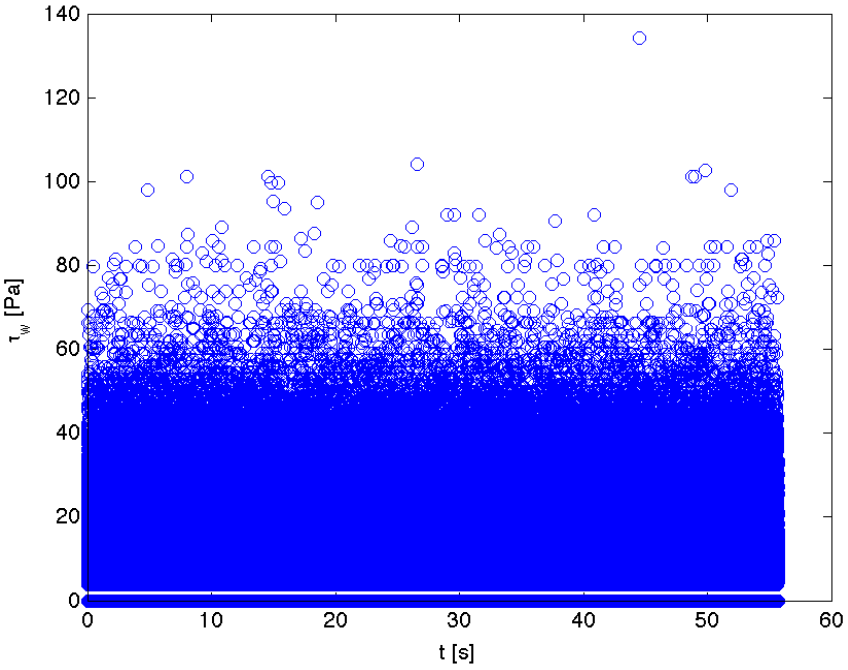

Figure A.3: *Raw data for pump frequency 40kHz*

Figure A.4 shows the relationship between signal to noise ratio (SNR) and the shear stress measured. There are few samples with good quality. We sampled for 1 minute and got only 50 quality measurements. This is a problem, since the goal is to measure turbulence in breaking waves, which is highly dependent on time. The sample frequency needs to be high enough so a true mean can be established from the measurements. The figure also shows that measurements with high shear stress have a low SNR. This means that the credibility increases as the shear stress decreases. It would be desirable with a SNR peak.

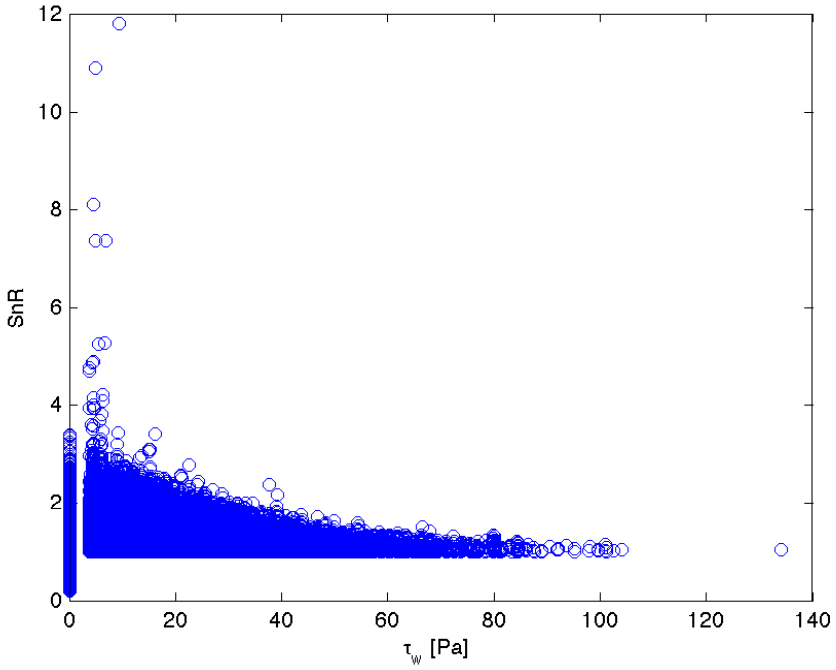

Figure A.4: SNR data for pump frequency 40kHz

Figure A.5 shows the wall shear stress measured compared with Blasius curve.

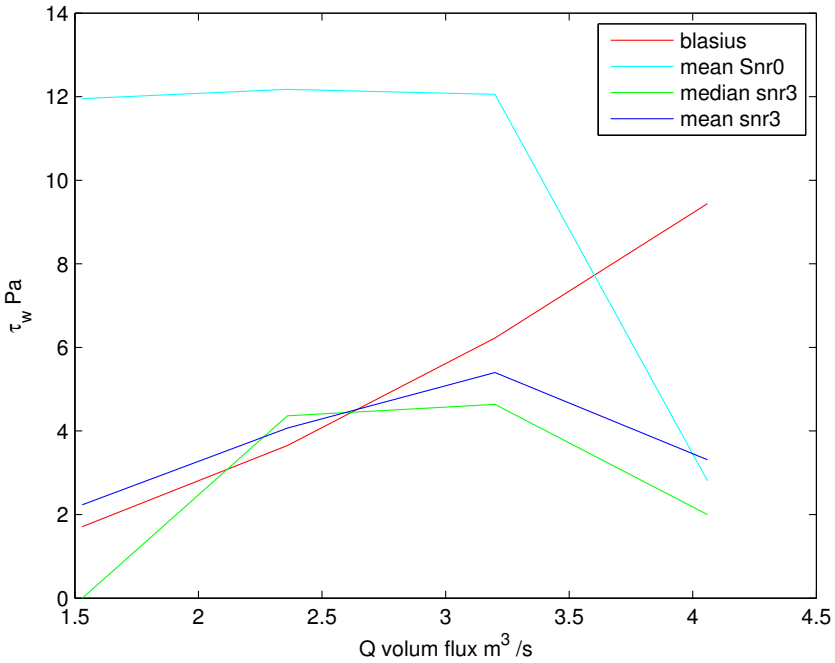

Figure A.5: *Filtered data*

The raw data signal does not fit Blasius curve at all. The measurement fits better when the data is filtered for low SNR, but then the lack of samples makes the mean and median differ from each other. This means that not enough data is gathered, and the credibility of the measurement drops. The measurement is still not according Blasius curve.

A.5 Remarks and conclusion

The main problem with the MicroS shear stress probe was the varying sample frequency. I believe that this is due to a leakage of laser light at the end of the wire connecting the hardware box and the probe. The wire glowed in the dark when the ceiling light was shut off. The leakage seemed to increase as the wire got curved. The MicroS shear stress sensor is an extremely sensitive instrument, which is a major drawback.

The other problem with the MicroS shear stress probe is the range it can measure. The lowest value it can measure is 0.7Pa in water. The highest Reynolds number one can have without turbulence is about 2300. From the definition of Reynolds number A.1, an equation for the

pipe diameter can be provoked:

$$D = \frac{Re}{\overline{u}} \frac{\mu}{\rho} \tag{A.11}$$

The definition of skin friction factor can be rearranged such that an equation for the mean velocity is obtained, where the laminar skin friction factor is found from equation A.6.

$$\overline{u} = \sqrt{\frac{2\tau_w}{\rho C_f}} = \sqrt{\frac{2\tau_w}{\rho \frac{16}{Re}}} = \sqrt{\frac{\tau_w Re}{8\rho}} \tag{A.12}$$

Substitution of $\overline{u}$ into equation A.13 gives

$$D = \frac{\mu\sqrt{8Re}}{\sqrt{\tau_w \rho}} \tag{A.13}$$

Both μ and ρ are constants, and the right hand side of the equation above is largest when the shear stress τ_w is smallest (0.7Pa) and the Reynold number is largest (2300). If the pipe is filled with water and the temperature is about $20°C$, then $\rho = 1.027 \cdot 10^3 \frac{kg}{m^3}$ and $\mu = 1.002 \cdot 10^{-3} \frac{kg}{sm}$, the diameter of the pipe must be $D < 0.005m$. This means that a pipe with a diameter of 5mm is needed for the shear stress probe to measure laminar flow. The problem is that the instrument itself will not fit in to a pipe of this size. The sensor will have problems measuring laminar water flow, regardless of horizontal velocities and the roughness of the pipe. This makes it hard to validate measurements against the analytical Hagen-Poisellieu solution.

Appendix B

Post processing of external data

The results presented in this section, is provided by use of Particle Image Velocimetry (PIV) and Particle Tracking Velocimetry (PTV).

B.1 Comparison of MatPIV and DigiFlow's PIV of linear waves

To compare MatPIV developed by J. Kristian Sveen and DigiFlow developed by Dalziel Research Partners, images of linear wave is used. The images is the same as used in Sveen (2004). The FOV is $30cm \times 30cm$, and a coordinate image is used to relate pixel displacement to real displacement. The results are then compared to linear wave theory B.1. If the surface elevation η is given as in B.1, a velocity potential ϕ can be derived from the equation in Chapter 2.

$$\begin{aligned} \eta &= a\sin(kx - \omega t) \\ \phi &= -\frac{a\omega}{k\sinh(kH)} cosh(k(z+H))cos(kx - \omega t) \end{aligned} \tag{B.1}$$

MatPIV uses a window shifting method where the size of the subwindows are altered, while DigiFlow shifts the location of the subwindows dynamically. The best results were obtained when DigiFlow's subwindow size was set to 16×16 pixels. The result is shown in Figure B.1.

The velocity profiles are obtained underneath the wave crest. Both MatPIV and DigiFlow find a horizontal and vertical velocity close to theory. Both methods underestimate the velocity in the horizontal direction. This is probably due to the image quality, or the fact that linear waves are ideal situations, where friction and surface tension is

neglected. The vertical calculated velocity should be equal to zero. The velocities are really small and this gives an indication of the error related to the experiment and method.

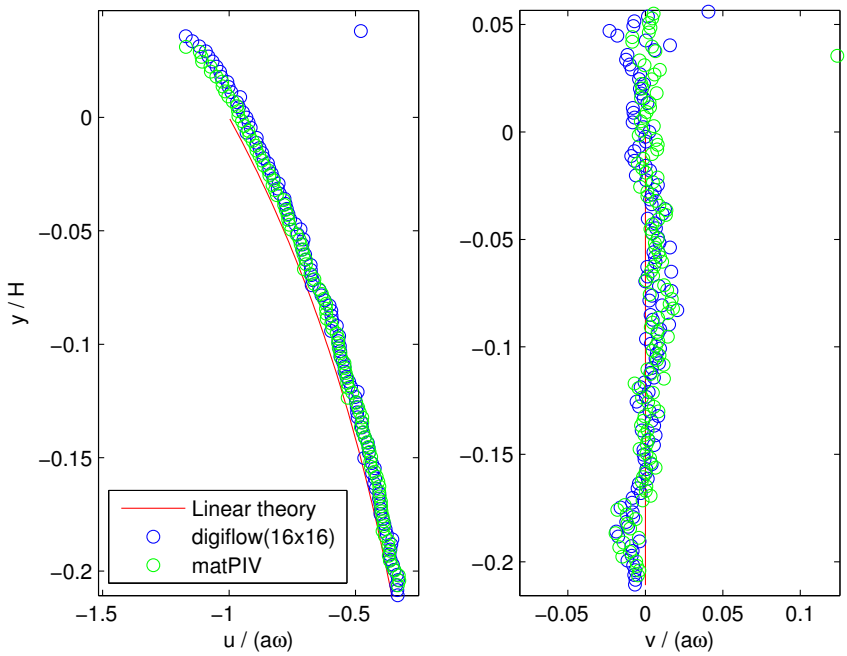

Figure B.1: *Comparison of MatPIV and DigiFlow's PIV*

B.2 Acceleration and velocities in breaking waves in the surf zone.

PIV and PTV are used to post process images of breaking waves, where the experiment was performed by Atle Jensen. The experimental set-up and condition are given in Mo et al. (2013). A list of the most important variables from the experiment is listed in table B.2.

	A/H=0.33	**A/H=0.50**
Amplitude m A	0.06	0.10
Sample freq camera Hz	1080	1080

B.2.1 Development of plunging breakers

The goal in this section is to find velocity profiles as close as possible to the wave front. We want to establish information on why waves develop the plunger shape.

The post processing for PIV was analysed with DigiFlow. There were three repetitions for the case A/H=0.33. The subwindow size was 16×16 pixels, and an overlap of 50% was used, giving a total of 128×128 vectors. A local filter was applied where data three standard deviations away from the mean was rejected. An average over the three repetitions was done where the median was used. The relative error was calculated by:

$$e_i = \frac{u_i - u_{mean}}{u_{mean}} \tag{B.2}$$

	Repetition 1	**Repetition 2**	**Repetition 3**
t_1	1.94%	1.82%	1.78%
t_2	3.18%	0.82%	0.92%
t_3	3.80%	17.8%	1.26%

Table B.1: *Repetition errors for PIV measurements*

The overall error is sufficient, but we have some problems in the region near the surface. Reflection of particles makes it hard to establish the actual surface line. The data is then smoothed by a linear Savitzky-Golay filter with a frame size of 5.

The PTV was processed with DigiFlow where particles with size [3-10] pixels was included. A Savitzky-Golay smoothing filter was first applied, where the frame size was set to 5 and the polynomial order was 2. The given position of the wanted velocity vector was determined by the PIV vectors closest to the wave front. A particle with a distance of 2% (of the images) from this x, was included in the grid making. Then data from three runs were put together. A *least square method* was used, where 21 particles were included for each grid point, hence ideally 7 from each run. The least square method solves equation B.3 for x, which gives the velocity at the given grid point.

$$A^T A\hat{\mathbf{x}} = A^T\mathbf{v} \tag{B.3}$$

However, the best approximation was made when the polynomial order

was set to 1.

Figure B.2a shows the location of the velocity profiles in figure B.2b, hence the blue, red and green profiles position are $[-13.94, -12.42, -9.67]$cm. One difficulty with these plots is that the flow is strongly dependent on both time and space, which makes it hard to smoothen the data. Another problem is that the number of particles close to the wave front is small. This gives us a small data set and the plots can easily be affected by artefacts. The velocity profiles in figure B.2a shows that velocities behave like vortices with a radial increasing strength, in addition to a uniform horizontal wave speed c.

B.2.2 Acceleration in plunging breakers

The goal in this section is to investigate acceleration in the plunge. PTV was performed with the same parameter as in the section above for the case A/H=0.50. Particles with a long trajectory in time were selected (Figure B.3). For each time-frame the median of the acceleration of all nearby particles was calculated. All particles within a distance of 0.5cm were included. The amount of particles considered in the median were few, since the trajectories were close to the wave front, see Table B.2.

Particle track	Blue	Red	Green	Black	Cyan
Number of particles	7.12	8.53	10.5	9.64	12.42

Table B.2: *Average number of particles participate in the median acceleration.*

A smoothing in time was also applied. The polynomial order was 2, and the frame size varied for each particle track (Table B.3).

Particle track	Blue	Red	Green	Black	Cyan
Frame size	21	23	15	17	7

Table B.3: *The frame size applied in the Savitzky-Golay filter.*

The wave profile and particle tracks are shown in Figure B.3. The squares in the figures correspond to the location at the different times.

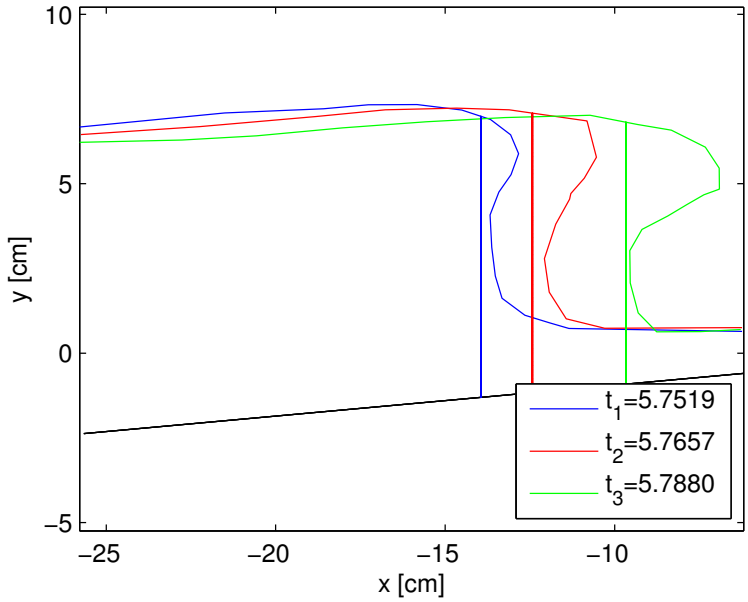

(a) *Surface profiles of development of plunger.*

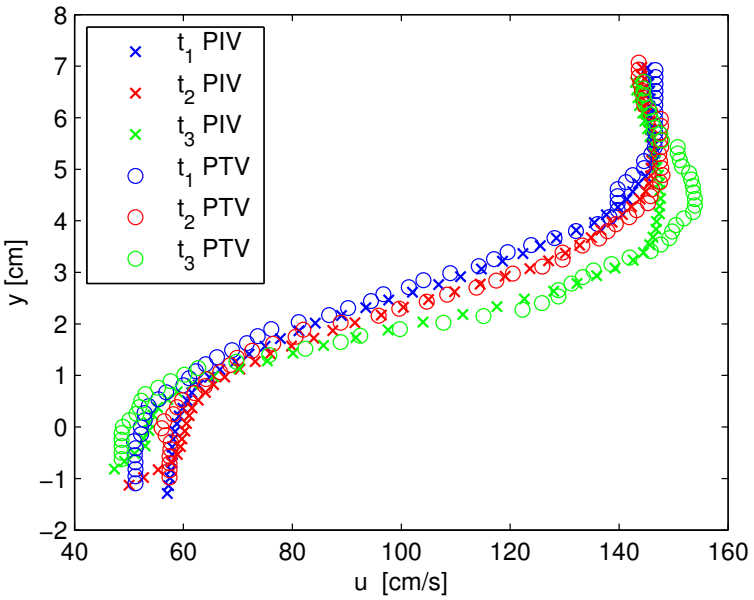

(b) *Velocities profiles near the steep wave front.*

Figure B.2: *Development of plunging breakers, A/H=0.33.*

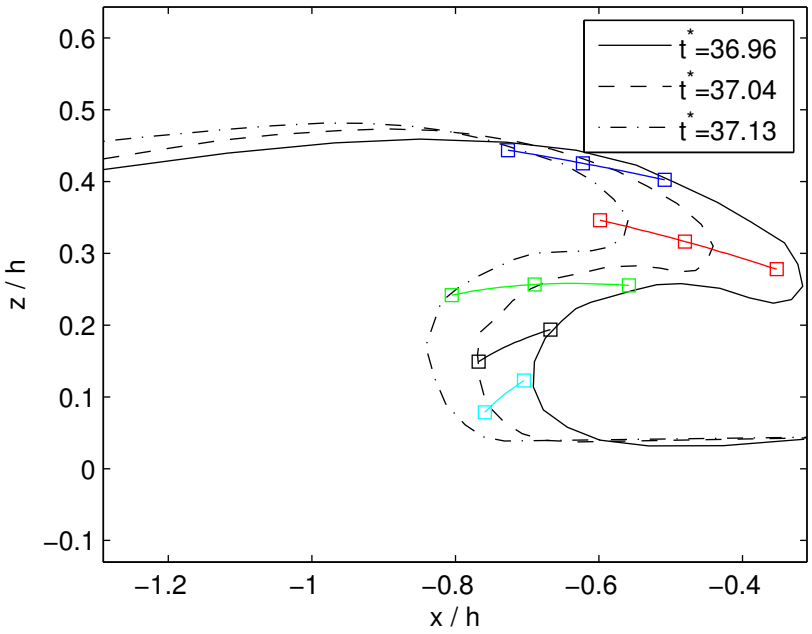

Figure B.3: *Particle trajectories and surface profiles.*

The acceleration calculated is shown in Figure B.4. Each color corresponds to the track of the same color as in Figure B.3. The most dramatic acceleration is not in the plunge itself, but at the wave front below the plunge. Acceleration as big as $4G$ is measured and strong forces are acting on the fluid.

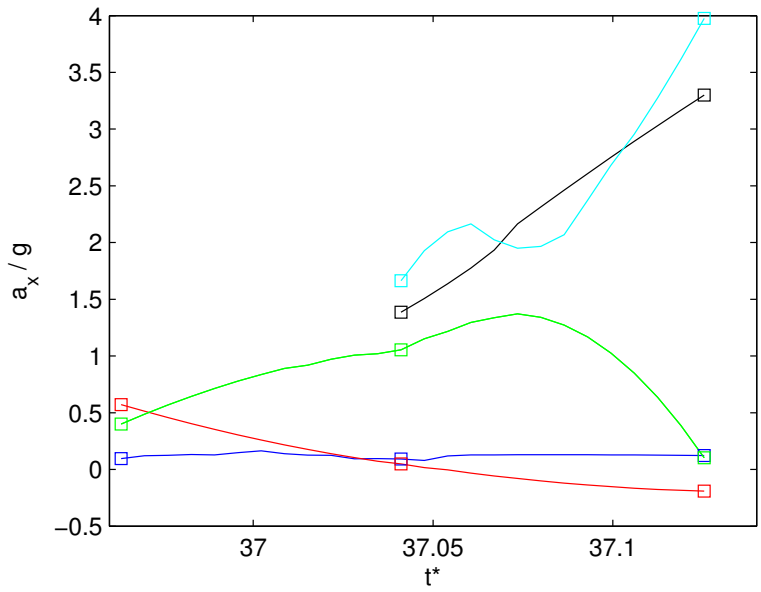

(a) *Horizontal acceleration*

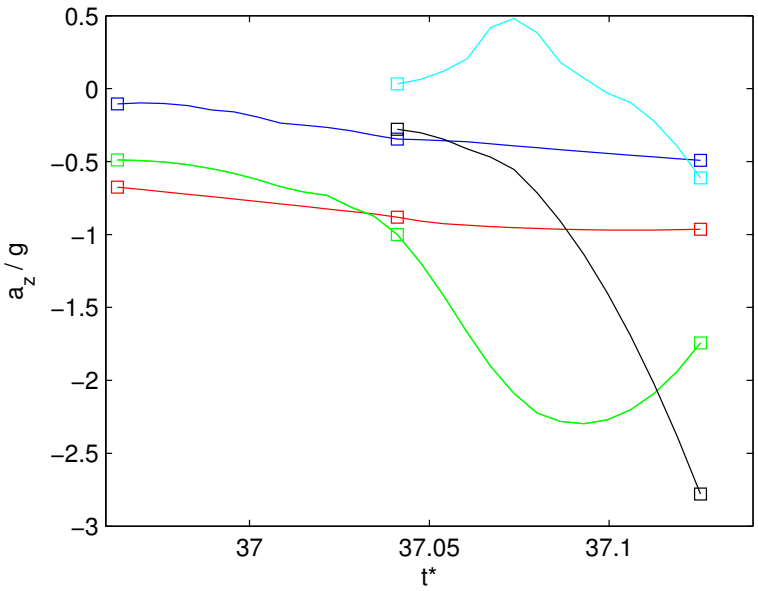

(b) *Vertical acceleration*

Figure B.4: *Acceleration for case50*

Bibliography

Banner (2010), 'U-gage s18u sensors with analog put', `http://info.bannerengineering.com/cs/groups/public/documents/literature/110738.pdf`. [Online; accessed 1-Aug-2014].

Barnes, M. P., O'Donoghue, T., Alsina, J. and Baldock, T. (2009), "Direct bed shear stress measurement in bore-driven swash", *Coastal Engineering* .

Beck, S. and Collins, R. (2008), Moody diagram, Technical report, Technical report, University of Sheffield.

Christensen, E. D. and Deigaard, R. (2001), "Large eddy simulation of breaking waves", *Coastal Engineering* , Vol. 42, Elsevier, pp. 53–86.

Cokelet, E. (1977), "Breaking waves", *Nature* , Vol. 267, pp. 769–774.

Colebrook, C. F. (1939), "Turbulent flow in pipes, with particular reference to the transition region between the smooth and rough pipe laws.", *Journal of the ICE* , Vol. 11, Thomas Telford, pp. 133–156.

Cowen, E. A., A.M.ASCE, Sou, I. M., A.M.ASCE, Liu, P. L.-F., F.ASCE and Raubenheimer, B. (2003), "Particle image velocimetry measurements within a laboratory-generated swash zone", *J. Eng. Mech* .

Dalziel, S. B. (1992), "Decay of rotating turbulence: some particle tracking experiments", *Applied Scientific Research* .

Dalziel, S. B. (2006), 'Digiflow user guide', `http://www.damtp.cam.ac.uk/lab/digiflow/digiflow.pdf`. [Online; accessed 20-Aug-2014].

Dictionary.com Unabridged (2014).
URL: *http://dictionary.reference.com/browse/surf-zone*

Elfrink, B. and Baldock, T. (2002), "Hydrodynamics and sediment transport in the swash zone: a review and perspectives", *Coastal Engineering* , Vol. 45, Elsevier, pp. 149–167.

Fenton, J. (1972), "A ninth-order solution for the solitary wave", *Journal of fluid mechanics* , Vol. 53, Cambridge Univ Press, pp. 257–271.

Gjevik, B., Pedersen, G. K. and Trulsen, K. (2010), *Lecture Notes Mek 4320 Hydrodynamic Wave theory*, University of Oslo.

Grass, A., Simons, R., Maciver, R., Mansour-Tehrani, M. and Kalopedis, A. (1995), "Shear cell for direct measurement of fluctuating bed shear stress vector in combined wave current flow".

Grilli, S., Svendsen, I. and Subramanya, R. (1997), "Breaking criterion and characteristics for solitary waves on slopes", *Journal of waterway, port, coastal, and ocean engineering* , Vol. 123, American Society of Civil Engineers, pp. 102–112.

Jensen, A., Pedersen, G. K. and Wood, D. J. (2003), "An experimental study of wave run-up at a steep beach", *Journal of Fluid Mechanics* , Vol. 486, Cambridge Univ Press, pp. 161–188.

Kikkerta, G., O'Donoghue, T., Pokrajacb, D. and Dodd, N. (2011), "Experimental study of bore-driven swash hydrodynamics on impermeable rough slopes", *Coastal Engineering* .

Kundu, P., Cowen, I. M. C. and Dowling, D. R. (2012), *Fluid mechanics fifth edition.*

Lindstrøm, E. K. (2011), "Run-up of solitary waves".

Mo, W., Jensen, A. and Liu, P. L.-F. (2013), "Plunging solitary wave and its interaction with a slender cylinder on a sloping beach", *Ocean Engineering* , Vol. 74, Elsevier, pp. 48–60.

Modarress, D., Fourguette, D., Tuagwalder, F., Gharib, M., Forouhar, S., Wilson, D. and Scalf, J. (2000), Miniature and micro-doppler sensors, *in* 'Proc. 10th Int. Symp. on Applications of Laser Techniques to Fluid Mechanics (Lisbon, Portugal, 10–13 July 2000)'.

Moody, L. F. (1944), "Friction factors for pipe flow", *Trans. Asme* , Vol. 66, pp. 671–684.

O'Donoghue, T., Pokrajac, D. and Hondebrink, L. (2010), "Laboratory and numerical study of dambreak-generated swash on impermeable slopes", *Coastal Engineering* , Vol. 57, Elsevier, pp. 513–530.

Pedersen, G., Lindstrøm, E., Bertelsen, A., Jensen, A., Laskovski, D. and Sælevik, G. (2013), "Runup and boundary layers on sloping beaches", *Physics of Fluids (1994-present)* , Vol. 25, AIP Publishing, p. 012102.

Peregrine, D. H. (1983), "Breaking waves on beaches", *Annual Review of Fluid Mechanics* , Vol. 15, Annual Reviews 4139 El Camino Way, PO Box 10139, Palo Alto, CA 94303-0139, USA, pp. 149–178.

Petti, M. and Longo, S. (2001), "Turbulence experiments in the swash zone", *Coastal Engineering* .

Rivillas-Ospina, G., Pedrozo-Acuña, A., Silva, R., Torres-Freyermuth, A. and Gutierrez, C. (2012), "Estimation of the velocity field induced by plunging breakers in the surf and swash zones", *Experiments in fluids* , Vol. 52, Springer, pp. 53–68.

science enterprise Inc, M. (2014), 'A micro-optical sublayer profilometer and shear stress sensor', `http://measurementsci.com/papers/microS_brochure.pdf`. [Online; accessed 20-Aug-2014].

Smithson, P., Addison, K. and Atkinson, K. (2002), *Fundamentals of the physical environment*, Psychology Press.

Sveen, J. and Cowen, E. A. (2004), *Quantitative imaging techiques and their application to wavy flows.*

Sveen, J. K. (2004), "An introduction to matpiv v. 1.6. 1", *Preprint series. Mechanics and Applied Mathematics http://urn.nb.no/URN:NBN:no-23418* .

Tanaka, M. (1986), "The stability of solitary waves", *Physics of Fluids (1958-1988)* , Vol. 29, AIP Publishing, pp. 650–655.

Viscous fluid flow (2006), chapter 3-3.1.

Wu, X. and Moin, P. (2008), "A direct numerical simulation study on the mean velocity characteristics in turbulent pipe flow", *Journal of Fluid Mechanics* , Vol. 608, Cambridge Univ Press, pp. 81–112.